Monte Carlo Simulations of Detector Prototypes Designed in a 65 nm CMOS Imaging Process

Sara Ruiz Daza

Masterarbeit in Physik
angefertigt im Physikalischen Institut

vorgelegt der
Mathematisch-Naturwissenschaftlichen Fakultät
der
Rheinischen Friedrich-Wilhelms-Universität
Bonn

November 2022

I hereby declare that this thesis was formulated by myself and that no sources or tools other than those cited were used.

Bonn, ...
Date Signature

1. Gutachterin: Prof. Dr. Ingrid-Maria Gregor
2. Gutachter: Prof. Dr. Jochen Dingfelder

Abstract

Monolithic CMOS sensors enable the development of detectors with a low material budget and a low fabrication cost. Moreover, using a small collection electrode results in a small sensor capacitance, a low analogue power consumption, and a large signal-to-noise ratio. These characteristics are very attractive in the development of new silicon sensors for charged particle tracking at future experiments. One of the goals of the Tangerine Project is to develop a test beam telescope setup consisting of detector prototypes designed in a novel 65 nm CMOS imaging process. This contribution describes the first steps and results in the design of such a telescope using the Allpix Squared and Corryvreckan frameworks for simulation and analysis. Furthermore, the thesis includes a discussion about the performance of the Tangerine sensors in a high occupancy situation, and validation of the parameters used in the simulations.

Contents

Introduction

Solid state semiconductor detectors have been used in High Energy Physics since the early 1980s. They achieve excellent position resolution by exploring structured electrodes such as pixels. Silicon pixel detectors are currently used in many particle experiments, and foreseen in future upgrades and experiments.

Pixel detectors can be made as hybrid or monolithic devices. In hybrid pixel detectors, sensor and readout electronics are separated into two different silicon blocks that are connected via bump bonds. Alternatively, monolithic detectors present the sensor and readout electronics integrated into one silicon block. The latter reduces the production cost, and the material budget, which is desired in tracking applications. In addition, monolithic pixel detectors with a small collection electrode results in a small sensor capacitance and a large signal to noise ratio.

At the Deutsches Elektronen-Synchrotron (DESY), the Tangerine Project exploits these capabilities to develop new silicon detectors that can be used at future lepton or electron-ion colliders. Currently, the project is investigating monolithic active pixel sensors (MAPS) in a novel 65 nm CMOS imaging process, being the first application of this technology in particle physics. The primary goal of the project is to design and develop a sensor that can be used at beam telescopes at DESY, demonstrating the capabilities of the 65 nm CMOS imaging process in high energy physics.

MAPS have a very complex electric field inside the pixel cell, therefore simulations are required to understand how charge carriers are transported and collected, and optimize the sensor designs. Detailed electric field simulations inside a pixel cell can be performed using Technology Computer-Aided Design (TCAD) [1]. Moreover, electric fields in TCAD can be used as input for other simulation tools, such as the Allpix^2 framework [2]. This combination of TCAD and Allpix^2 results in high-statistic, fast, flexible, and precise Monte Carlo simulations of silicon detectors. Allpix^2 also allows for more complex systems, such as test beam telescopes where the analysis can be performed with the Corryvreckan framework [3].

This report starts with an introduction to silicon detectors in Chapter 1. Chapter 2 and 3 describe the simulation and analysis workflow with Allpix^2 and Corryvreckan. The Tangerine Project and the sensor layouts studied in this work are presented in Chapter 4. Chapter 5 summarizes the optimization studies and validation of the sensor simulations using Allpix^2. The performance of the sensors in a high occupancy situation is discussed in Chapter 6. Finally, Chapter 7 shows the first results of the Tangerine beam telescope simulations.

CHAPTER 1

Silicon Detectors for Particle Physics

When a particle traverses a material, they interact, i.e. the particle deposits energy in the medium. Particle physics detectors exploit these interactions to identify and infer particle properties such as momentum, charge, energy, velocity, et cetera. Semiconductor detectors measure the deposited energy to provide information on the impinging particles. The following chapter summarizes the interaction of particles with matter and the working principle of semiconductor detectors with a focus on silicon sensors.

1.1 Interaction of Particles with Matter

The most dominant processes of interaction of charged particles with matter are ionization and excitation, Bremsstrahlung, and multiple Coulomb scattering.

1.1.1 Ionization and excitation

For heavy charged particles, the mean energy loss from ionization and excitation per traversed length dE/dx is described by the Bethe-Bloch formula:

$$-\left\langle \frac{dE}{dx} \right\rangle = 4\pi N_A r_e^2 m_e c^2 \frac{Z}{A}\rho\frac{z^2}{\beta^2}\left[\frac{1}{2}\ln\frac{2m_e c^2\beta^2\gamma^2 T_{max}}{I^2} - \beta^2 - \frac{\delta(\beta\gamma)}{2} - \frac{C(\beta\gamma, I)}{Z}\right] \tag{1.1}$$

where N_A is Avogadro's number, r_e the classical electron radius, m_e the electron mass, A and Z the atomic mass and atomic number of the absorber, z the charge of the incident particle, β the velocity as a fraction of the speed of the light of the incident particle, γ the Lorentz factor, T_{max} the maximum energy transfer in a single collision, I the mean excitation energy of the medium, $\delta(\beta\gamma)$ the density correction at high energies, and $C(\beta\gamma, I)$ the shell correction at low energies [4].

The Bethe-Bloch region extends in the range $0.1 \lesssim \beta\gamma \lesssim 1000$. In this region, the energy losses via ionization and excitation are dominant. For $\beta\gamma \sim 3{-}4$ the energy loss reaches the minimum. Particles around this global minimum are called *minimum ionizing particles (MIPs)*. Typical values of the mean energy loss (or deposited energy) per unit thickness in silicon for MIPs are ~388 eV µm [5].

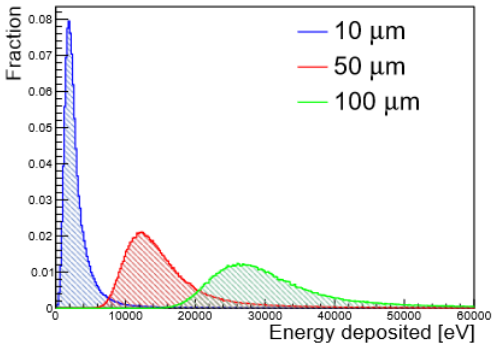

Figure 1.1: Deposited energy for a 5 GeV single-electron beam in 10, 50 and 100 µm of silicon. The simulation is performed using the GEANT4 and Allpix^2 frameworks.

Landau distribution

The statistical fluctuations of energy loss around the mean value given by Equation 1.1 are described by a Landau distribution [6]. Due to the long tail of this distribution, the most probable value is smaller than the mean value. Figure 1.1 shows the energy deposited distribution for a 5 GeV single-electron beam in 10, 50 and 100 µm of silicon. For thinner sensors, the most probable value shifts to the left.

The main contribution to the long tail are the so-called *δ-electrons* or *knock-on electrons*. These δ-electrons are kicked-off from the atoms as the result of an inelastic electron collision between the incoming particle and the atom. The kinetic energy of the ejected δ-electrons depends on the emission angle. For larger angles, the kinetic energy is smaller. Since most of the δ-electrons are emitted perpendicular to the direction of the incoming particle, they have low kinetic energy, that results in large energy losses (see Equation 1.1). They move away from the track, contributing to ionization and degrading the spatial resolution.

1.1.2 Bremsstrahlung

The electromagnetic radiation (photon emission) due to the interaction of a charged particle with an atomic nucleus is called bremsstrahlung, and it is the dominant source of energy loss at high energies. The energy loss due to bremsstrahlung is inversely proportional to the squared particle mass. Therefore, for particles with a low mass (e.g. electrons and positrons), bremsstrahlung is the dominant source of energy loss, even at low energies.

The *critical energy* is defined as the energy where the losses through ionization and bremsstrahlung are equal. For electrons in silicon, the critical energy is 40.2 MeV [5].

The path length traveled by an electron through a material that loses all but $1/e$ of its initial energy is called *radiation length* X_0. In silicon, the radiation length is 9.36 cm [5].

1.1.3 Multiple Coulomb Scattering

Charged particles crossing a material are scattered randomly multiple times, mainly due to interactions with the Coulomb fields of atomic nuclei in the material. This stochastic process is known as *multiple scattering* and it is unwanted in tracking applications since it changes the particle direction, deteriorating the spatial resolutions and momentum.

Assuming small deflection angles, the scattering angle θ distribution can be described by a Gaussian, which standard deviation σ_θ is given by

$$\sigma_\theta = \frac{13.6\,\text{MeV}}{\beta c p} z \sqrt{\frac{x}{X_0}} \left[1 + 0.038 \ln\left(\frac{x}{X_0}\right) \right] \tag{1.2}$$

where p and z are the momentum in MeV and charge of the scattered particle, and x and X_0 the thickness and radiation length of the traversed material [4]. Thus, the influence of multiple scattering is reduced for large particle momenta and low material budget (x/X_0).

1.2 Semiconductor detectors

In solid-state physics, the band structure of a solid is described by the electronic band theory. The electronic band theory is based on quantum mechanics and describes the energy range that an electron within the solid may have [7].

At temperature $T = 0\,\text{K}$, the highest energy band completely filled with electrons is called *valence band* and the band directly above in energy is called *conduction band*. The highest occupied energy level at $T = 0\,\text{K}$ defines the Fermi level. Electrons excited from the valence band to the conduction band, as well as holes left in the valence band, contribute to the electrical conductivity.

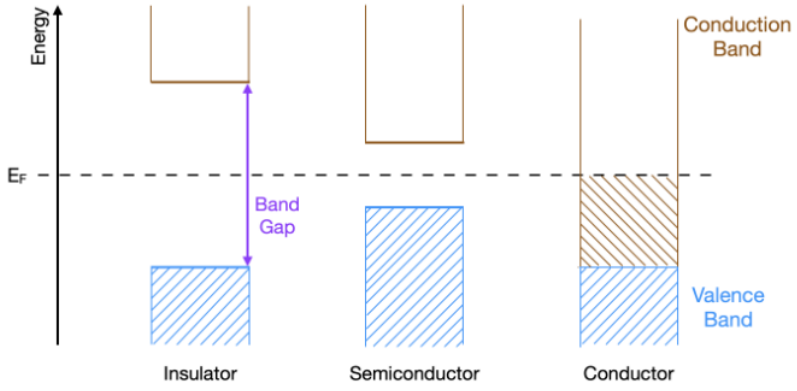

Figure 1.2: Energy band diagrams for conductors, semiconductors and insulators.

Figure 1.2 shows the conduction and valence band configurations for insulators, semiconductors and conductors. For a conductor, the valence and conduction bands overlap. For an insulator, the distance between both bands (*band gap*) is very large and thermal excitation is not sufficient to excite electrons to the conduction band. In the case of insulators and pure semiconductors (non-doped or *intrinsic semiconductors)*, the Fermi level lies in the middle. At $T = 0\,\mathrm{K}$, an intrinsic semiconductor behaves as an insulator. However, semiconductors have a smaller band gap, meaning that, at higher temperatures, thermal excitation is enough to excite electrons into the conduction band. The band gap for silicon at room temperature is 1.12 eV.

The conduction properties of intrinsic semiconductors can be modified by introducing impurity atoms. A doped semiconductor is called *extrinsic semiconductor*. While the atoms stay neutral, the electron and hole concentrations changes and the Fermi level is shifted. A *n-type* semiconductor is doped with electron donor atoms, electrons become the majority charge carriers and the Fermi energy is shifted closer to the conduction band. A *p-type* semiconductor is doped with electron acceptor atoms, holes become the majority charge carriers and the Fermi energy is shifted closer to the valence band. For silicon, typical n-type dopants are phosphorus or arsenic and p-type dopants are boron or gallium.

1.2.1 pn junction

When p- and n-doped semiconductor materials are brought together, a pn junction is formed. Without an applied voltage, free electrons from the n-side diffuse into the p-side and recombine with holes. Similarly, holes in the p-side diffuse into the n-side and recombine with electrons. Thus, at the boundary, a so-called *depletion region* without mobile charge carriers is formed. Moreover, now the n-side has a positive *space-charge* density, whereas the p-side has a negative *space-charge* density. As a result, an intrinsic electric field counteracting the diffusion forms. This potential difference is called *built-in potential* or *diffusion voltage* V_D.

If a reverse bias V_{bi} is applied (the n-side is connected with the positive terminal and the p-side is connected with the negative terminal of a voltage source), electrons in the n-side and holes in the p-side are pulled away from the pn boundary and the size of the depletion region is increased. A reverse bias on a pn junction diode constitutes the basis of most semiconductor detectors.

The neutral condition (in the space-charge, the number of charge carriers on the n-side is the same as in the p-side) implies that the depletion region extends deeper towards the more weakly doped region. Assuming that the doping concentration of the n-type is much larger than of the p-type ($N_D \gg N_A$), the depletion-zone width d increases with stronger biases and lower N_A concentrations, and can be estimated as:

$$d \approx \sqrt{\frac{2\epsilon\epsilon_0}{e}(V_D + V_{bi})\frac{1}{N_A}} \tag{1.3}$$

where ϵ and ϵ_0 are the permittivities of the semiconductor and the vacuum respectively. Equation 1.3 can be also expressed in terms of the wafer resistivity ρ as:

$$d \propto \sqrt{\rho V_{bi}} \tag{1.4}$$

1.2.2 Charge formation and collection

When a charged particle crosses the detector or a photon is absorbed, electron-hole pairs are generated. The required mean energy for the creation of an electron-hole pair in silicon at room temperature is 3.65 eV [5]. Since part of this energy goes to phonon excitations of the lattice, this energy needs to be larger than the the band gap for silicon (1.12 eV). Therefore, the number of electron-hole pairs n_{eh} created by a traversing particle is given by

$$n_{eh} = \frac{E_{\text{deposited}}}{3.65\,\text{eV}} \tag{1.5}$$

where $E_{\text{deposited}}$ is the deposited energy of the incoming particle. For a traversing MIP, approximately 70 electron-hole pairs are created per micrometer in silicon. These charge carriers drift following the electric field lines towards the collection electrodes. The drift velocity v_D is given by

$$v_D = q\mu(E)E \tag{1.6}$$

where q is the charge sign and μ is the charge carrier mobility that depends not only on the electric field but also on the temperature, the doping concentrations, and the type of charge carrier (electron/hole). The electron and hole mobility can be described by different models such as the Jacoboni-Canali [8], the Hamburg Model [9], the Masetti Model [10] or the Arora Model [11]. Moreover, the Jacoboni-Canali and Masetti models can be combined [12], and the mobility is parametrized as:

$$\mu(E, N) = \frac{\mu_m(N)}{\left(1 + (\mu_m(N) \cdot E/v_m)^\beta\right)^{1/\beta}} \tag{1.7}$$

with μ_m the Masetti mobility [10], and v_m and β parameters defined by the Jacoboni-Canali model [8].

Besides drift, the charge carriers in silicon also move randomly. This effect is known as *diffusion* and leads to charge clouds that slowly and isotropically grow in size. The charge cloud can be modelled as a function of the time t by Gaussian distribution with width σ_{diff}

$$\sigma_{\text{diff}} = \sqrt{2Dt} \tag{1.8}$$

where D is the diffusion constant given by the Einstein equation:

$$D = \frac{k_B T}{q}\mu \tag{1.9}$$

where k_B is the Boltzmann constant and is T the temperature.

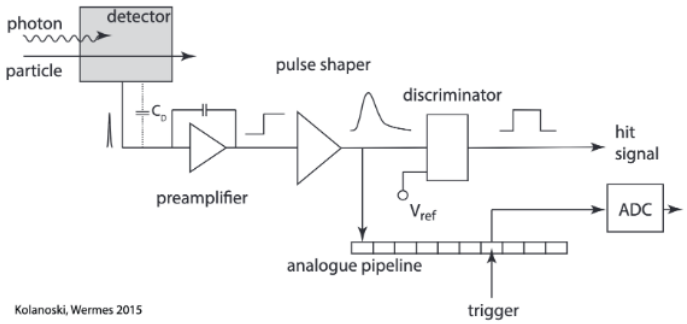

Figure 1.3: Sketch of a typical front-end readout. From [4].

Charge carriers can be generated/recombined as a consequence of intermediate defects levels in the silicon bad gap. The recombination of charge carriers can be modeled mathematically by Shockley-Read-Hall [13] model, the Auger [14] model, and by a combination of both statistical models (SRH-Auger model) [12].

1.2.3 Signal processing and detector readout

Once the charge is collected, an electronic circuit (front-end) is needed for the readout and processing of the signal. The front-end components depend on the type of detector. A sketch of a typical front-end is shown in Figure 1.3. Firstly, the signal is processed by the preamplifier which amplifies the signal, and by the shaper that returns the pulse to the baseline after a finite time avoiding pile-up of signals. Then, the discriminator compares the signal hit to a reference value provided (detection threshold). If this analog signal is above the detection threshold, the signal can be digitized by the analog-to-digital converter (ADC). In the case that the signal needs to be stored before digitization, sequential buffers (pipelines) can be introduced.

1.2.4 Hybrid Pixel Detectors

In hybrid pixel detectors, the sensor (particle sensing element) and the readout chip (electronics circuitry) are bump-bonded together, as illustrated on the left side of Figure 1.4. That means that both parts can be developed, tested, and optimized individually, and only connected in a last step with the flip-chip bonding technique [15]. As a consequence, a fast charge collection of the order of a few nanoseconds and high levels of radiation tolerance can be achieved. Besides this, hybrid pixel detectors can have a large signal-to-noise ratio (SNR), allowing the operation of the detector at high thresholds without noise while keeping high efficiency.

Disadvantages of the hybrid technology are related to the bump-bonding technology. The flip-chip bonding process is very complex and expensive. Moreover, it enlarges the material budget and multiple scattering contributions, limiting the tracking accuracy. Also, it limits the achievable pixel pitch because bump bonds cannot be made arbitrarily small.

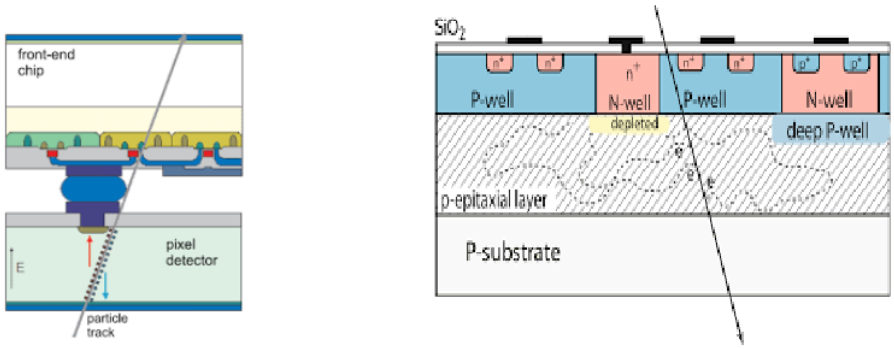

Figure 1.4: Cross section of a hybrid pixel cell (left) and of a monolithic active pixel cell (right). From [4].

1.2.5 Monolithic Active Pixel Sensors

In contrast to hybrid pixel detectors, monolithic pixel sensors contain the particle sensing and the signal processing elements in one silicon block, reducing the production cost and complexity. Thin sensitive sensor volumes can be achieved, decreasing the material budget, and thus the influence of multiple scattering and secondary interactions in tracking applications. Small pixel sizes and high granularity detectors can be achieved, improving the spatial resolution.

In this thesis, monolithic active pixel detectors (MAPS) with small collection electrodes are studied. A sketch of a cross-section of a MAPS is shown in Figure 1.4. It contains full CMOS circuitry, and a thin p-epitaxial layer grown on a low-ohmic p-substrate. Charges are collected only by the n-well collection electrode. The other n-well that contains PMOS transistors is shielded by the deep p-well from the sensor, protecting the electronics and ensuring no charge collection. Without an external electric field applied (only the intrinsic electric field due to the built-in potential is present) or a small voltage applied, a small depletion between the n-well and p-epitaxial layer is created and the collection of charges is dominated by diffusion.

As charges are collected mainly by diffusion, the monolithic technology is sensitive to displacement damage, being this the main historic drawback of this technology. Also, slow charge collection by diffusion results in a worse timing performance. According to Equation 1.4, the depletion region, and thus the collection of charges via drift can be enhanced by increasing the bias voltage or using a higher resistivity p-substrate. The maximum bias voltage that can be applied is limited by the electronics. Numerous studies are ongoing, including sensor layout modifications (see Section 4), to enhance the depletion volume, timing performance, and radiation tolerance of MAPS [16, 17].

During the last long shutdown at the LHC, the ALICE ITS was upgraded with seven concentric layers of ALPIDE MAPS [18], covering a total active surface of $\sim 10\,\mathrm{m}^2$, this being an example of a large scale experiment using MAPS with a small collection electrode. With this approach, the sensor fulfilled the experimental requirements of having a power consumption

of less than 40 mW cm^{-2}, efficiency above 99%, spatial resolution better than 5 µm, and being radiation hard up to $1{\times}10^{13}$ n_{eq} cm^{-2}. For the next upgrade, ALICE is developing a bent-silicon vertex tracker consisting of very thin (20-40 µm) MAPS [19].

The 65 nm CMOS Imaging Technology

The novel 65 nm CMOS imaging process allows for a higher in-pixel logic density. Thus, it reduces the space needed for the transistors and increases the in-pixel functionality. As a consequence, the pixel pitch can be reduced (10-35 µm), improving the spatial resolution. The collection electrode size can be reduced as well. CMOS pixel detector designs with a small collection electrode result in small sensor capacitance, low analog power consumption, and a large signal-to-noise ratio. The Tangerine Project at DESY is currently investigating this process in particle physics applications (see Chapter 4).

CHAPTER 2

Monte Carlo Simulations: From a Single Sensor to a Beam Telescope

This chapter describes the necessary steps to simulate a beam telescope, starting from single-sensor simulations. The simulation flow of the investigated sensors and beam telescope has three components:

- For the MAPS investigated in this work (see Chapter 4), the small collection electrode design results in a strongly non-linear and complex electric field that needs to be simulated precisely. To do so, generic doping profiles are used to perform three-dimensional Technology Computer-Aided Design (TCAD) simulations of pixel cells. By numerically solving Poisson's equation for electrostatic potential, TCAD provides highly accurate electric fields inside the pixel cell. Figure 2.1 illustrates the complex electric field inside the sensor for one of the studied layouts. This part is not covered in the work presented here [20].
- The generic doping profiles and TCAD electric fields are imported into Allpix^2 [2]. The Allpix^2 framework allows for complete and fast Monte Carlo simulations of a sensor, including charge deposition, carrier propagation and simplified front-end electronics response. More complex systems can be also simulated, such as the beam telescope that is described in this chapter.
- The Corryvreckan framework is used to analyze the beam telescope data [3]. It can be easily integrated with Allpix^2. More details about this are given in Chapter 3.

2.1 Monte Carlo simulations

Sensor performance could be studied very precisely only by means of TCAD tools. However, its high computational cost and time-consuming simulations make this approach of only using TCAD tools impractical. To reduce simulation time while maintaining high accuracy, a simpler charge carriers propagation algorithm can be used, like the one implemented in Allpix^2. This algorithm

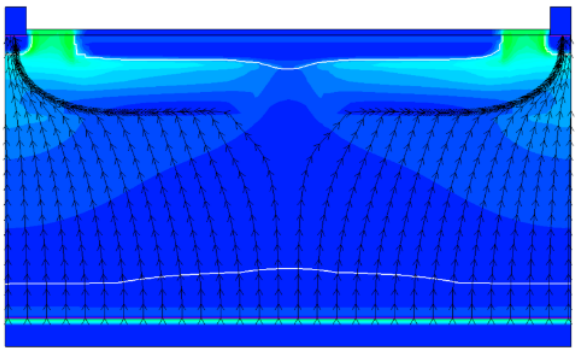

Figure 2.1: TCAD simulation of the n-gap layout (see Chapter 4). The streamlines of the electric field are represented in black and the edges of the depletion region in white. The collection electrodes are in the corners. From [21].

accounts for the effects like the Landau fluctuations in the energy deposition stage, formation of δ-electrons, and propagation of charges via drift and diffusion. In this way, by importing the TCAD fields and running simulations with Allpix^2, high-statistics samples (that are required for sensor characterization) can be obtained in a shorter amount of time.

2.2 Introduction to Allpix^2

Allpix^2 is a generic, easy to use and open-source simulation framework for semiconductor detectors. It is written in C++, and together with GEANT4 [22] and ROOT provides a flexible and powerful toolset to study the energy deposition, charge propagation, signal transfer, and digitization in a sensor. The structure of the Allpix^2 framework is illustrated in Figure 2.2. The Allpix^2 core (on the left) handles the common utilities of the modules (on the right) which implement the simulation process. This chapter focuses on the description of the modules and their parameters.

Two coordinate systems are defined in Allpix^2: the local coordinate system and the global coordinate system. Both are right-handed Cartesian systems. The local coordinate system is defined for each simulated detector, and the origin is in the center of the lower left pixel in the matrix. In the work presented here, the matrix of pixels is defined by the pixelization of a single plane. The x- and y-axis are then defined in the direction of the next pixel in the matrix (to the right and up), and the z-axis with the depth of the sensor. The global coordinate system is useful when several detectors (each with a different local system) are simulated, for example a beam telescope, since it helps to reconstruct the trajectory of the particle in an external and unique coordinate system. Transformations from local to global coordinate systems, and vice versa, can easily be done [2].

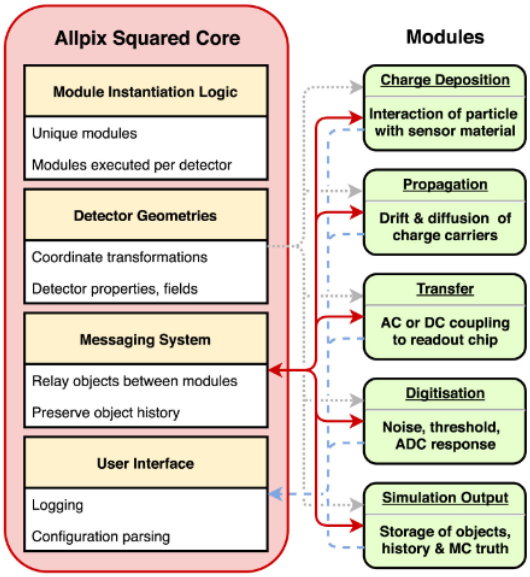

Figure 2.2: Structure of the Allpix^2 framework. From [2].

2.3 Simulation flow

To run a simulation in Allpix^2, three configuration files are needed: the *main configuration*, the *detector model configuration* and the *geometry configuration*. Below, a brief description of these configuration files and the modules used for this work is given. A more detailed description can be found in the manual of Allpix^2 [12]. The parameters in the modules are finalized for this work after the studies presented in Chapter 5.

2.3.1 Detector model configuration

The detector model configuration describes the type of detector simulated. The parameters provided are:

- `type`: either a monolithic or hybrid detector;
- `number_of_pixels`: number of pixels in the x and y directions;
- `pixel_size`: pitch of the pixel in x and y directions;
- `sensor_thickness`: thickness of the sensor (in z direction);
- `implant_size`: collection electrode size in x and y;
- `sensor_excess`: extra passive material added to the pixel matrix on the top, bottom, left and right directions.

An example of a configuration file (named `20um_pitch.conf`) used in the simulations presented in this work is:

```
type = "monolithic"
number_of_pixels = 20 20
pixel_size = 20um 20um
sensor_thickness = 50um
implant_size = 2.2um 2.2um
sensor_excess = 200um
```

2.3.2 Geometry configuration

The geometry configuration defines the geometry of the simulated setup. Some basic parameters are:

- `type`: the detector model configuration;
- `position`: 3D position in the global coordinate system;
- `orientation`: 3D rotation angles.

An example of a geometry configuration for a sensor is given below:

```
[dut]
type = "20um_pitch"
position = 0 0 0
orientation = 0 0 0
```

In the case of a full telescope simulation (see Chapter 7, the `number_of_pixels` in the detector model configuration can be adapted to the desired value, and several planes can be replicated in the geometry configuration file. In addition, for each of the telescope planes and the DUT (Device Under Test), random misalignments (in position and orientation) can be introduced using the parameters:

- `alignment_precision_position`: width of the Gaussian distribution in x, y and z from which a random misalignment shift is drawn;
- `alignment_precision_orientation`: width of the Gaussian distribution in the three rotation angles from which a random misalignment shift is drawn.

An example of a geometry configuration (named `detector.conf`) for six telescopes planes and an inactive silicon box representing a DUT in the center is given below. Figure 2.3 illustrates the visualization of this configuration in GEANT4.

```
[telescope0]
type = "20um_pitch"
position = 0um 0um 0mm
orientation = 0deg 0deg 180deg
alignment_precision_position = 1mm 1mm 100um
alignment_precision_orientation = 0.2deg 0.2deg 0.2deg

[telescope1]
type = "20um_pitch"
position = 0um 0um 150mm
...

[telescope2]
type = "20um_pitch"
position = 0um 0um 300mm
...

[dut]
type = "box"
position = 0um 0um 450mm
orientation_mode = "xyz"
orientation = 0deg 0deg 180deg
size = 30mm 30mm 50um
material = "silicon"
role = "passive"

[telescope3]
type = "20um_pitch"
position = 0um 0um 600mm
orientation_mode = "xyz"
...
[telescope4]
type = "20um_pitch"
position = 0um 0um 750mm
...

[telescope5]
type = "20um_pitch"
position = 0um 0um 900mm
...
```

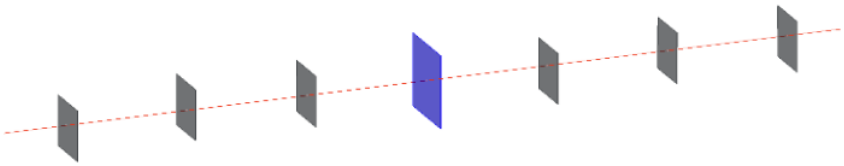

Figure 2.3: GEANT4 visualization of the simulated beam telescope and the DUT (inactive silicon box in the center). In red, one 5 GeV single-electron event crosses the setup. The visualization is obtained with the `[VisualizationGeant4]` module in Allpix^2.

2.3.3 Main configuration

A typical semiconductor detector simulation flow with Allpix^2 is followed in this project. Figure 2.4 illustrates this workflow and includes the names of the modules used. Additional modules such as the `[DetectorHistogrammer]` and `[VisualizationGeant4]` are also useful during the preliminary studies, as they provide a basic inspection of the performance of the detector and a display of the constructed GEANT4 geometry respectively (Figure 2.3). In this project, to perform a more precise and flexible examination, the data are stored and externally analyzed with ROOT and Corryvreckan. The analysis chain is presented in Chapter 3.

In the following, an introduction of the models, with their parameters, is given. Examples of configuration files are included as well.

Global configuration

The global configuration under the header `[Allpix]` contains the global parameters of the framework:

- `detectors_file`: path to the geometry configuration;
- `model_path`: path to the detector model configuration;
- `multithreading`: enable or disable the parallel execution of event simulations;

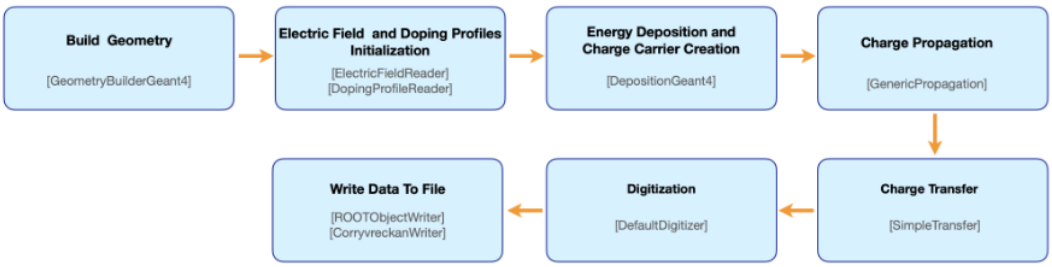

Figure 2.4: Typical simulation flow with Allpix^2.

- `output_directory`: path to the directory where the output files are stored;
- `root_file`: name of the output ROOT file containing the configuration information and output plots;
- `number_of_events`: number of simulated events.

```
[Allpix]
detectors_file = "telescope.conf"
model_paths = "20um_pitch.conf"
multithreading = true
output_directory = "output"
root_file = "telescope.root"
number_of_events = 250000
```

GEANT4 geometry

The `[GeometryBuilderGeant4]` module constructs the GEANT4 environment. The `world_material` should either be air or vacuum.

```
[GeometryBuilderGeant4]
world_material = "air"
```

Energy deposition

The `[DepositionGeant4]` module handles the energy deposition in the active volume of all detectors, and the charge carrier creation. It initializes the particle source that deposits energy. There are several predefined sources, but a GEANT4 macro can also be used. In this work, a 5 GeV single-electron Gaussian spread beam is simulated. The deposited energy is converted into charge carriers using Equation 1.5, and fluctuations are modeled with the Fano factor. The Photoabsorption Ionization Model (PAI) can be included to improve the model describing the ionization energy loss in very thin materials [23]. For the Tangerine sensors, the following parameters are used:

- `physics_list`: GEANT4 physics process list;
- `number_of_particles`: number of particles simulated in a single event;
- `particle_type`: type of GEANT4 particle to use;
- `source_energy`: mean kinetic energy of a particle;
- `source_type`: type of sources: beam, point, square, sphere or macro;
- `source_position`: position of the particle source;
- `beam_size`: width of the Gaussian beam profile, only for source "beam" selected;
- `beam_direction`: direction of the incident particle beam, only for source "beam" selected;

- `max_step_length`: maximum length of a simulation step in the sensitive volume (since this only sets a limit, it does not correspond to the distance between charge depositions, but also not to the maximum of this distance because charges could be deposited at intermediate steps, see Section 5.2);
- `enable_pai`: the PAI model can either be enabled or disabled.

A typical example of configuration is:

```
[DepositionGeant4]
physics_list = FTFP_BERT_LIV
number_of_particles = 1
particle_type = "e-"
source_energy = 5GeV
source_type = "beam"
source_position = 0um 0um -20mm
beam_size = 100um
beam_direction = 0 0 1
max_step_length = 1um
enable_pai = true
```

Electric field and doping profile initialization

An electric field can be applied within the sensor. This field can be linear, parabolic, constant, customized or imported (for example, from TCAD). The latter model receives the name of `mesh`, and is used in this work. The mesh adaptation from TCAD into Allpix^2 is done with the `Mesh Converter` module in Allpix^2, and more details are given in Section 5.1. The parameters used are:

- `model`: type of the electric field model;
- `file_name`: path to the imported electric field;
- `field_offset`: shift of the field to correct the center of coordinate system from the imported framework into Allpix^2.

An example of configuration file is:

```
[ElectricFieldReader]
model = "mesh"
file_name = "ElectricField.apf"
field_offset = 0.5,0.5
```

Similarly, the doping profiles can be imported from TCAD. An example of configuration file is:

```
[DopingProfileReader]
model = "mesh"
file_name = "DopingConcentration.apf"
field_offset = 0.5,0.5
```

Propagation of charge carriers

The `[GenericPropagation]` module simulates the propagation (drift and diffusion) of charge carriers through a sensor. A fourth-order Runge-Kutta-Fehlberg method [24] is used to calculate the particle equations of motion in the defined electric field. After every Runge-Kutta step, the random diffusion is accounted for by applying an offset drawn from Equation 1.8. The propagation of the charge carriers finishes when they reach any surface of the sensor.

This module is very flexible, and its parameters can have a strong impact on the duration and precision of the simulations, as will be discussed in Chapter 5. The parameters used in this work are:

- `temperature`: temperature of the device;
- `charge_per_step`: maximum number of charge carriers propagated as a group in the same position;
- `timestep_min`: minimum step in time to use for the Runge-Kutta integration;
- `timestep_max`: maximum step in time to use for the Runge-Kutta integration;
- `integration_time`: time window within which the charge carriers are propagated;
- `recombination_model`: charge carrier recombination model;
- `mobility_model`: charge carrier mobility model;
- `propagate_type`: electrons and/or holes can be propagated.

An example of configuration is:

```
[GenericPropagation]
temperature = 293K
charge_per_step = 5
timestep_min = 0.5ps
timestep_max = 0.05ns
integration_time = 25ns
recombination_model = "srh_auger"
mobility_model = "masetti_canali"
propagate_electrons = true
```

Charge transfer

The `[SimpleTransfer]` module transfers the signal from the sensor to the readout electronics. After the integration time, all charge carriers located within the collection electrode boundary, defined by the `implant_size` in the detector model configuration and the `max_depth_distance` explained below, are grouped together and sent to the front-end electronics.

- `max_depth_distance`: maximum distance in depth from the sensor surface within which propagated charge carriers are collected;
- `collect_from_implant`: set to true to collect only charge carriers within the collection electrode instead of the full surface of the sensor.

A example of configuration is:

```
[SimpleTransfer]
max_depth_distance = 0.55um
collect_from_implant = true
```

Digitization stage

The `[DefaultDigitizer]` module simulates the response of the front-end electronics. The parameters used in this work are:

- `threshold`: detection threshold for a hit to be detected in electrons;
- `electronics_noise`: standard deviation of the Gaussian noise added to the signal before applying the threshold, in electrons;
- `threshold_smearing`: standard deviation of the Gaussian uncertainly in the threshold, in electrons;
- `qdc_resolution`: resolution of the charge-to-digital converter (QDC) in bits;
- `qdc_slope`: slope of the QDC calibration;
- `qdc_offset`: offset of the QDC calibration.

The QDC resolution depends on the front-end electronics design and is a known parameter. A `qdc_resolution` equal to 6 bits can encode $2^6 = 64$ distinct characters (ones and zeros). The conversion from electron (e) units to QCD units is done as

$$\text{charge(QDC)} = \frac{\text{qdc\_offset(e)} + \text{charge(e)}}{\text{qdc\_slope(e)}} \tag{2.1}$$

where the charge is the collected charge in electrons, and the chosen `qdc_slope` and `qdc_offset` depends on the region of the Landau distribution that is to be covered, and therefore on the application. If, for example, the Landau peak is to be sampled precisely, and the long tail is not considered interested, according to Figure 1.1, a good charge window to sample would be from 100 (detection threshold value) to 1 500 electrons. This corresponds to a charge range of 1 400

electrons and a `qdc_offset` of −100 electrons. Using a QDC resolution of 6 bits, each digit will encode the information of 1 400/64 ∼20 electrons. Thus, in this particular case, a `qdc_slope` of 20 electrons is selected.

An example of simple digitization is:

```
[DefaultDigitizer]
threshold = 100e
threshold_smearing = 0e
electronics_noise = 0e
```

Writing data to file

The simulation information can be stored in ROOT objects for external analysis. This can be done with the `ROOTObjectWriter` module. Different objects can be included in the ROOT file:

- MCTrack: Monte Carlo truth initial and final state in global coordinates of the incoming particle. The initial and final positions, energies, the creation process type, name, volume, and the particle ID (using the PDG particle codes [5]) are stored.
- MCParticle: Monte Carlo truth information in global and local coordinates of the particle. The arrival position and time in the sensor, the exit position at the sensor edge, the particle ID and reference to the associated MCTrack are stored.
- DepositedCharge: information of the charge carriers deposited in the sensitive material. The charge deposition position in local coordinates, the time, and the carrier type are stored.
- PropagatedCharge: information of the charge carriers propagated through the sensor. The final position in local coordinates and timing information of collected or recombined charge carriers are stored.
- PixelCharge: information of the set of charge carriers collected per pixel. The pixel indices and the total number of charge carriers collected are stored.
- PixelHit: digitised pixel hit information processed by the front-end electronics. The time and signal information stored depends on the type of digitiser simulated.

An example of configuration is:

```
[ROOTObjectWriter]
include = "PixelHit", "MCParticle", "PixelCharge"
file_name = data_telescope
```

Furthermore, the full beam telescope data can be stored for future analysis with Corryvreckan, in the correct data format by using the `[CorryvreckanWriter]` module. One plane, acting as reference plane during the analysis, and the DUT, should be marked. This module creates a

detector configuration file and ROOT file with the simulation information that are imported into Corryvreckan. An example of configuration is:

```
[CorryvreckanWriter]
file_name = corryvreckan
output_mctruth = true
reference = "telescope0"
dut = "dut"
```

An output example of the detector configuration file is in Appendix A.

CHAPTER 3

Tracking with a Beam Telescope

This chapter describes the reconstruction steps performed to find the trajectory of a particle that crosses several detector planes. Starting from the reconstructed hit position in each of the planes, the trajectory of the particle is inferred. In particle physics, this process is known as tracking. In this work, tracking is performed with a simulated beam telescope setup. Since accurate simulations are achieved with Allpix^2, the data analysis is performed in a similar way to how real data would be treated. Thus, the reconstruction chain presented in this chapter can be applied to both real data and simulations. Furthermore, the framework used, Corryvreckan [3], is also extensively employed in real test beam data reconstruction. Therefore not only very accurate simulations are achieved, but also a realistic reconstruction is performed.

3.1 Test beam telescopes

Test beam facilities provide high energetic particle beams that can be used to test and characterize new sensor prototypes. Few test beam facilities can be found worldwide, one example is the DESY II Test Beam Facility [25] in Hamburg, Germany.

A particle beam coming from an accelerator enters the test beam area, in which a beam telescope and a device under test (DUT) are placed. A typical beam telescope configuration has the DUT in the middle between three telescope planes upstream and three telescope planes downstream, as illustrated in Figure 3.1. The telescope planes act as reference planes and reconstruct the trajectory of the particle (track). By comparing the track intersection with the DUT and the reconstructed DUT position, efficiency and resolution studies can be performed. These analyses are described in the following sections.

3.2 Cluster reconstruction

The traversing particles can induce a signal in more than one collection electrode due to the effect of charge sharing among adjacent pixels. The charge sharing effect can be caused by diffusion movement of carriers inside the sensor, by carrier drift inside the sensor in the presence of an

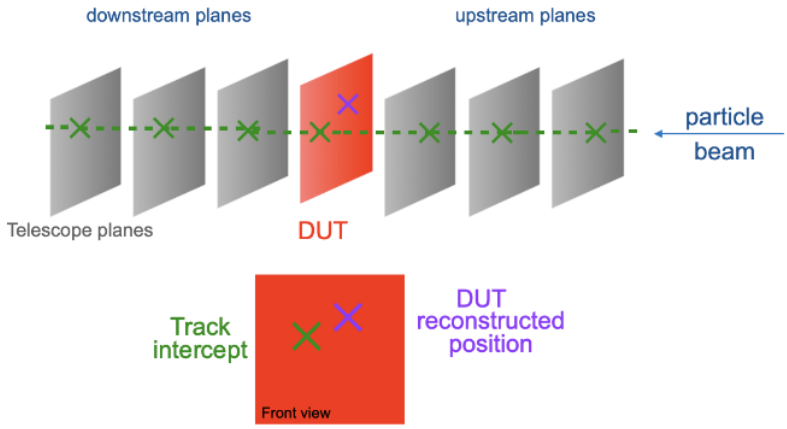

Figure 3.1: Test beam telescope sketch. In green, the track reconstructed using the hit information from the telescope planes is shown. In magenta, the reconstructed position by the DUT.

electromagnetic field, or by inclined particle incidence. For large pixel sizes and thick sensors, it is common to tilt the sensor a few degrees to increase this effect. However, for thin sensors, like the ones investigated in this work (see Section 4), the increase of share sharing is insignificant when they are slightly rotated. Moreover, in this project, no external magnetic field is applied. Hence, diffusion is the major contribution to charge sharing.

A *cluster* is defined as a group of adjacent pixels that all have an induced charge above the threshold. The pixel with the highest charge in a cluster is called the *seed pixel*, and the number of pixels in a cluster defines the *cluster size*. The cluster size is highly dependent on the pixel geometry and the detection threshold.

If only one pixel fires (i.e. has an induced charge above the threshold), the cluster size is one, and the reconstructed cluster position is in the center of the pixel. However, if more than one pixel fires, the spatial cluster center reconstruction depends on the information available. In the case that the charge distribution over the matrix is available (in-pixel charge measurement), the cluster center is calculated with the conventional *center-of-gravity algorithm* (or *charge-weighed cluster algorithm*). The center-of-gravity algorithm does not only take the pixel position in the cluster $\vec{x}_i = (x_i, y_i)$ into account, but also how much charge is deposited in each of the pixels, q_i. Mathematically, the reconstructed cluster center position $\vec{x}_{clu} = (x_{clu}, y_{clu})$ can be expressed as follows:

$$\vec{x}_{clu} = \frac{\sum_i \vec{x}_i \, q_i}{\sum_i q_i} \tag{3.1}$$

For a binary readout, the cluster center position is directly determined at the average position of the pixel centers in the cluster (equivalent to consider $q_i = 1, \forall i$ in Equation 3.1). In the simulations presented in this work, the charge collected per pixel is available, and thus the center-of-gravity algorithm is used to reconstruct the cluster center.

3.3 η-correction

The cluster position reconstruction, based on finding the center-of-gravity, assumes a uniform charge sharing inside the sensor, and thus, that charge sharing is uniformly among adjacent pixels. However, for the sensors studied in this project, this is not true. The bulk modifications and the non-homogeneous electric field inside the sensor, that push charges towards the collection electrode, results in a nonuniform charge sharing between adjacent pixels. This implies that the reconstructed position is not accurate, and the so-called *η-correction* needs to be applied. The η-function defines the charge sharing distribution and is used for the correction.

Figure 3.2 illustrates this effect for three adjacent pixels in the x-direction. In the y-axis is plotted the relative charge collected per pixel 1 with respect to the total cluster charge. If the particle hits the pixel close to its center, no charge sharing takes place, and $Q_{\text{pixel 1}}/Q_{\text{cluster}}$ approaches one. Particles hitting the boundary between two identical pixels, will transfer half of the energy deposited to each of the pixels. However, in all other regions, the collected charge collected per pixel is different. A linear charge sharing assumption is marked with a blue line. In red, the η-function describes the real charge sharing effect in the x-axis. The shape of the η-function depends on the sensor geometry, electric field, doping concentration, and detection threshold. A more detailed description can be found elsewhere [26].

In simulations, this η-distribution in X and Y $\eta(\vec{v}) = \eta(v_x, v_y)$ can obtained with a fit of the reconstructed cluster position $\vec{x}_{clu} = (x_{clu}, y_{clu})$ as function of the true position for events with cluster size equal to two. With the this fit, the reconstructed cluster position is corrected. For tracking (and in Corryvreckan), the fit is directly obtained by comparing the track interception and the associated cluster center. All telescope simulations presented in this thesis include the η-correction.

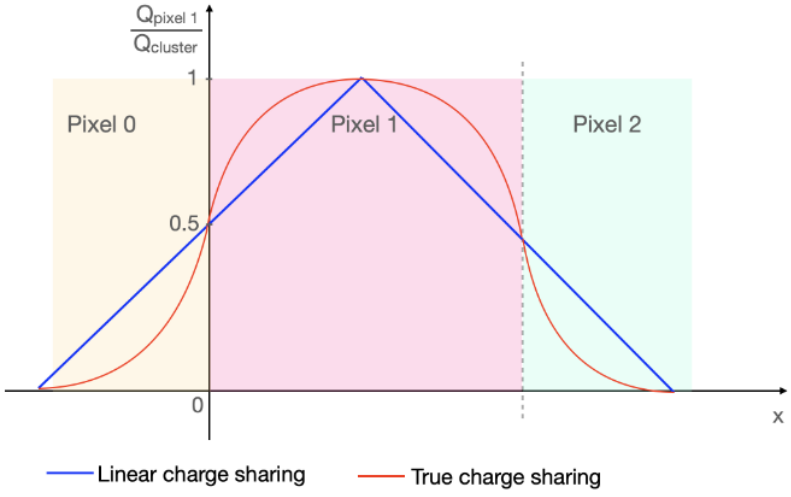

Figure 3.2: Charge sharing sketch for three adjacent pixels in the x-direction. The y-axis represents the fraction of the pixel 1 charge collected per cluster charge. The blue line assumes a linear charge sharing behavior. In red, the η-function that corrects for the non-linear charge sharing effect is shown.

3.4 Spatial resolution and detection efficiency

Two important quantities to characterize a semiconductor detector are the the *spatial resolution* and the *detection efficiency*.

Spatial resolution and residuals

The spatial resolution σ indicates how precise the position of a particle traversing a detector can be reconstructed. Smaller values for the spatial resolution are desired. For a binary readout, the intrinsic spatial resolution σ_{int} of a sensor is the pixel pitch divided by $\sqrt{12}$, given by the standard deviation of the uniform distribution of hits on the interval $[0, \text{pitch}]$. This value can be improved by allowing charge sharing between neighboring pixels and using the center-of-gravity method to reconstruct the cluster center, as explained previously.

In sensor simulations, the spatial resolution can be obtained from the distribution of the difference between the reconstructed cluster position (using the center-of-gravity algorithm) and the true Monte Carlo position. This difference is called *residual*. The standard deviation of the distribution of the residuals determines the intrinsic resolution of the sensor. As both the truth and the reconstructed positions are known precisely over the whole pixel, in-pixel resolution maps can be obtained.

A similar method can be used in test beam measurements to obtain the spatial resolution in any of the planes. In this case, the Monte Carlo truth data is replaced by the track intercept (reconstructed with the beam telescope) on that particular plane. Thus, the residuals are defined as the difference between the reconstructed track intercept on that plane and the reconstructed position of that plane, as illustrated in Figure 3.3. Depending on the way the tracks are reconstructed, two types of residuals can be defined: *biased residuals* and *unbiased residuals*. In biased residuals, r_b, the cluster on the plane is included in the track reconstruction, while in unbiased residuals, r_u, the cluster on the plane is excluded in the track reconstruction. From the width of the Gaussian distribution of the unbiased/biased residuals, the resolution $\sigma_u(z)/\sigma_b(z)$ at any plane is obtained. In this work, the spatial resolution is given by the root mean square of the central 99.73 % (i.e. central 3σ) of the residual distribution. It is related with the intrinsic resolution of the sensors as:

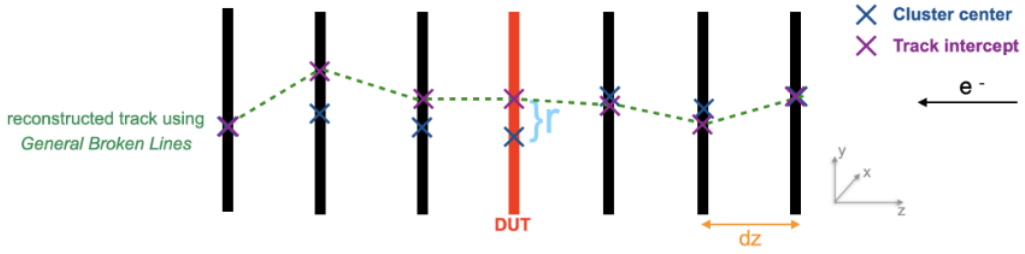

Figure 3.3: Sketch of the reconstructed cluster center position and their associated track center position. The difference between them determines the residuals.

$$\sigma_b^2(z) = \sigma_{\text{int}}^2 - \sigma_{t,b}^2(z) \tag{3.2}$$

$$\sigma_u^2(z) = \sigma_{\text{int}}^2 + \sigma_{t,u}^2(z) \tag{3.3}$$

where $\sigma_{t,b}(z)$ and $\sigma_{t,u}(z)$ are the biased and unbiased track resolutions at a position z respectively [27]. In a common test beam measurement, where the goal is to determine the intrinsic resolution of the DUT, $\sigma_{\text{int}}(z = \text{DUT})$, the unbiased method is followed. The $\sigma_{\text{int}}(z = \text{DUT})$ is obtained after measuring the residuals and subtracting the assumed (or measured) track resolution at the DUT position.

In this work, the goal is to design a beam telescope and determine its track resolution at any position. Therefore, as a first step, the intrinsic resolution of the sensors used is studied via sensor simulations. As a second step, the residuals are determined by simulating the full beam telescope.

Detection efficiency

The hit detection efficiency of a DUT is defined as the ratio between the number of events detected by the DUT and the true number of events crossing the DUT. It gives the probability of detecting a particle going thought the sensor. Values close to one are desired, i.e. measuring every track. In test beam measurements, this true number is provided by the telescope planes.

In the simulations presented in this work, two efficiencies are defined: *hit detection efficiency* and *beam telescope tracking efficiency*.

The hit detection efficiency in simulations is defined as the number of events detected by the sensor divided by the total number of simulated events that hit the sensitive area of the detector. To obtain the hit detection efficiency a matrix of 20×20 pixels is simulated.

In this work, the beam telescope tracking efficiency is determined by the ratio between the total number of reconstructed events by the beam telescope and the total number of simulated single-particle events.

Both the spatial resolution and the efficiency are important parameters to characterize the sensor performance. Apart from the detector geometry, they are also highly dependent on the bias voltages and detection threshold. According to Equation 1.3, higher bias voltages result in larger depletion regions and thus in the collection of more charges, improving the efficiency. Moreover, if the same amount of charge is distributed among several pixels, a high threshold results in lower efficiency, especially at the pixel edges and corners. This effect can be observed in Figure 3.4. The cluster size and in-pixel efficiency in four adjacent pixels for two different thresholds is shown. For a low threshold of 100 electrons, the cluster size is one in the central part of the pixel, while it is approximately two at the edges and four at the corners. The efficiency is almost one in all the parts of the pixel cell. For a larger threshold of 200 electrons, the cluster size is decreased in the edges and corners, and the efficiency starts to deteriorate.

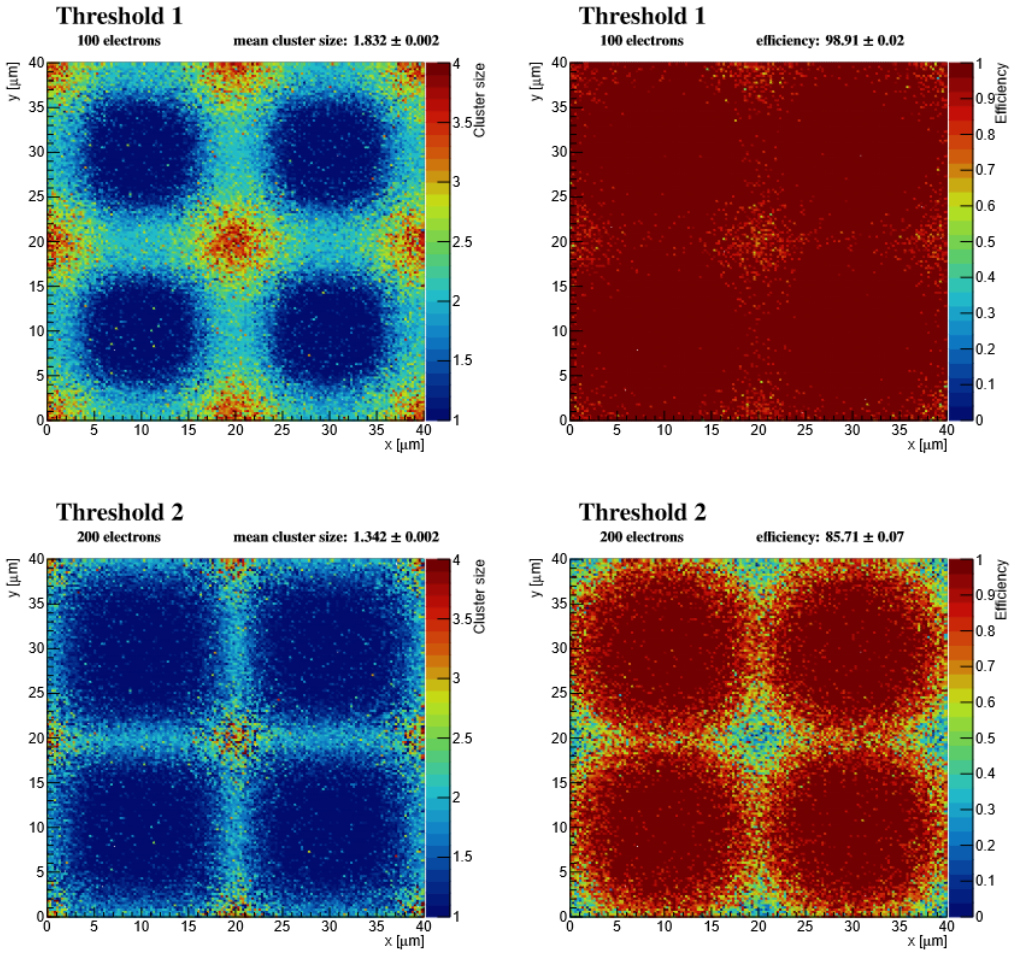

Figure 3.4: In the first column, the in-pixel cluster size plots for four adjacent pixels are shown. In the second column, the in-pixel efficiencies for four adjacent pixels are shown. The figures correspond to two different hit detection thresholds: threshold 1 (100 electrons) and threshold 2 (200 electrons) for the standard layout (see Chapter 4) with a pixel pitch of 20 µm.

3.5 Track reconstruction

The reconstruction of the trajectory of a charged particle traversing the beam telescope has two parts: track finding and track fitting.

Cluster centers from different planes within a defined spatial and time window are grouped together. The complexity of this process is given by the number of simulated particles going through the beam telescope and the information stored by the planes (time information available speed up the process by reducing the number of track candidates).

Then, the trajectory of the particle is determined from a fit to the cluster centers in the beam telescope planes. After the track fitting, the quality of the fit is determined by the global track algorithm in this work. The global track χ^2 divided by the number of degrees of freedom (ndof) with a peak close to one indicates a good track fit.

Different track models can be used to reconstruct the trajectory of the particle through the beam telescope. The simplest model assumes that the particle travels straight through the beam telescope, ignoring scattering. This approach is valid for high energy beam particles, with zero magnetic field applied, and low material budget detector planes. The χ^2 of a straight line using the reconstructed cluster centers can be calculated as:

$$\chi^2 = \sum_{p=0}^{N} \left(\frac{r_{p_x}^2}{\sigma_{p_x}} + \frac{r_{p_y}^2}{\sigma_{p_y}} \right) \tag{3.4}$$

where r_{p_x} and r_{p_y} are the residuals in the plane p in X and Y directions, and σ_x and σ_y are the intrinsic resolution in X and Y of the sensors in the planes.

General Broken Lines (GBL)

More sophisticated track fitting methods, that accounts for the multiple Coulomb scattering described in Section 1.1.3, are the Kalman filter [28] and the General Broken Lines (GBL) algorithm [29]. The latter method is used in this work. The GBL algorithm includes the scattering angles with the planes and air as additional track parameters, and computes the complete covariance matrix of all track parameters.

3.6 Beam telescope alignment

In test beam experiments, the mechanical alignment is not precise enough to get high-resolution tracks. Misalignment will lead to assuming the wrong positions of the detectors and thus of the particle hits. Therefore, alignment corrections need to be applied. The same is true for the simulations presented here, where random misalignment (in position and rotation) was applied for the telescope planes. The alignment correction of the beam telescope is done in two steps in this work: prealignment and final alignment.

The goal of the telescope prealignment is to minimize the mean of the residual distributions of the reconstructed positions between neighboring telescope planes. To do so, shifts along the X- and Y- axes are applied in software. While the telescope prealignment does not require tracking, the final alignment does and it is performed with respect to the selected reference plane. For each telescope plane, the position in X and Y and the three orientation degrees of freedom are iteratively varied, the tracks are refit, and the global track χ^2 is minimized. This minimization of χ^2 during alignment is done using the Minuit2 [30] algorithm.

3.7 Track reconstruction with Corryvreckan

The Corryvreckan framework [3] is a flexible, fast, and open-source test beam data reconstruction framework. Similar to Allpix^2, it is based on a modular concept, and both frameworks can be easily integrated together. As explained in Section 2.3.3, the `[CorryvreckanWriter]` module in Allpix^2 stores the output data and the geometry configuration file in a format that can be read by Corryvreckan. This section describes the full analysis chain of the simulated beam telescope with Corryvreckan. A more complete description can be found in the manual [31].

3.7.1 Geometry configuration

The position, detection, and properties of the detector planes are included in the geometry configuration file. An example is given in Appendix A. This configuration is generated automatically by Allpix^2, including the material budget of the detector layer. The intrinsic resolution of the sensors needs to be included manually, however. If it is not specified, the default value of pitch/$\sqrt{12}$ will be used, and consequently, for sensors with better resolution, the track χ^2 values will be wrongly computed after assuming the wrong uncertainly on the cluster centers. This value is determined by the sensor simulations and set with the `spatial_resolution` parameter for each of the planes in the geometry configuration file.

3.7.2 Global configuration

The global configuration file includes the modules followed by their parameters. Due to the different steps of prealignment, alignment, eta-correction for the hit position, and analysis, four different configuration files are necessary. A description of the modules included in such configuration files is given below. In the examples given, the parameters not included are left at their default values [31].

Global configuration

The first module, `[Corryvreckan]`, contains the global parameters:

- `detectors_file`: path of the detector configuration file;
- `detectors_file_updated`: path of the output detector file with the new configuration;
- `histogram_file`: path of the ROOT file in which the histograms of all the modules are stored;

- `number_of_events`: total number of events that will be processed.

In the following example, the detector configuration file named `corryvreckanGeometry.conf` is obtained with Allpix^2.

```
[Corryvreckan]
detectors_file = "corryvreckanGeometry.conf"
detectors_file_updated = "corryvreckanGeometry_aligntracks.conf"
histogram_file = "output_aligntracks.root"
number_of_events = 250000
```

Reading data from file

The second module, `[FileReader]`, reads the ROOT objects stored by Allpix^2. Its used parameters are:

- `file_name`: path of the ROOT data file;
- `include`: list of objects to be read from the ROOT file (see Section 2.3.3).

An example of configuration where the `corryvreckan.root` file is obtained with Allpix^2 is:

```
[FileReader]
file_name = "corryvreckan.root"
include =  "PixelHit", "MCParticle", "PixelCharge"
```

Cluster reconstruction

The `[Clustering4D]` module performs clustering of pixel data on all detectors. Either an arithmetic mean or the center-of-gravity algorithm can be selected with the `charge_weighting` parameter to reconstruct the cluster center. This module can also take advantage of time information if available, to only cluster pixels within a configurable time window.

An example of configuration where the center-of-gravity algorithm is used is:

```
[Clustering4D]
charge_weighting = true
```

Track reconstruction

In this work, the module `[Tracking4D]` is used for the track reconstruction. Similarly to the `[Clustering4D]` module, the time information stored for each hit can be included to improve the track finding process.

A first candidate straight-line track is reconstructed using only the cluster center from the first and last beam telescope planes. Then, associated clusters (within a defined time and position window) are found in the further planes and the track is updated.

The parameters used in this work are:

- `min_hits_on_track`: minimal number of associated clusters requested to create a track;
- `spatial_cut_abs`: maximum allowed distance between the cluster center and a track for association in X and Y defining an ellipse;
- `exclude_dut`: the DUT can be either included or excluded for track reconstruction;
- `track_model`: either the straight line or the GBL method used for track reconstruction;
- `momentum`: beam momentum required by the GBL algorithm.

In order to get high-quality tracks, the `spatial_cut_abs` parameter is set to four times the pixel pitch at the beginning and decreased incrementally down to the pixel pitch for each of the runs. In the following example, at least five planes (out of six) require hits for performing tracking:

```
[Tracking4D]
min_hits_on_track = 5
spatial_cut_abs = 80um, 80um
exclude_dut = true
track_model = "gbl"
momentum = 5GeV
```

Telescope alignment

The `[AlignmentTrackChi2]` module performs the alignment of the telescope planes. Alignment in position in X and Y and/or orientation over the three rotations can be selected with the parameters `align_position` and `align_orientation`. At the end, a sub-micrometer precision alignment is reached.

An example of configuration used in this work is:

```
[AlignmentTrackChi2]
align_position = true
align_orientation = true
```

Writing data to file

The `[FileWriter]` module stores in a ROOT file the "pixel", "cluster" and "track" objects for external analysis.

An example of configuration used in this work is:

```
[FileWriter]
file_name = "data.root"
include =  "Track", "Pixel", "Cluster"
```

Analysis

A useful module for the analysis of a beam telescope is `[AnalysisTelescope]`. This module computes the difference between the Monte Carlo particle position and track intercept at the DUT position. Its parameter `chi2ndof_cut` limits the χ^2/ndof for the track to be included in the analysis.

An example of configuration is:

```
[AnalysisTelescope]
chi2ndof_cut = 3
```

η-correction

In Corrryvreckan, the η-correction is performed only for cluster sizes of two in X and Y. Firstly, the positions of the cluster reconstructed and their associated track intercept are compared, and the η-correction formula is fitted. This is done with the `[EtaCalculation]` module, which returns the fit parameters. An example of module configuration is:

```
[EtaCalculation]
```

This example is running with the default parameters. In particular, a polynomial of fifth order is used as the fit function (eta-function). Other functions can be chosen with the `eta_formula_x`/`eta_formula_y` module parameters. It returns the fit parameters that are used as input by the `[EtaCorrection]` module. The `[EtaCorrection]` module applies this fit to correct the reconstructed cluster positions for all beam telescope planes.

CHAPTER 4

The Tangerine Project

The Tangerine Project (Towards Next Generation Silicon Detectors) aims for the development of new silicon detectors that can be used at future lepton or electron-ion colliders. A position resolution of around 3 µm, a time resolution below 10 ns, and a material budget of less than 0.05 % of a radiation length are typical requirements of these experiments. Radiation hardness is not a concern for these experiments.

Currently, the Tangerine project is investigating MAPS in a novel 65 nm CMOS imaging process, being the first application of this technology in particle physics and thus demonstrating its capabilities. The project comprises all the steps of sensor R&D: electronics design, sensor design based on TCAD and Monte Carlo simulations, as well as prototype testing. Sensor simulations, lab characterization and test beam measurements of the first test chip are ongoing [21, 32].

The initial goal of the Tangerine project is to develop a test beam telescope that can be used at the DESY II Test Beam facility. Chapter 7 summarizes the first simulations of such a setup, with a focus on optimizing the telescope geometry with respect to the tracking resolution.

Investigated sensor layouts

The sensors being developed in the Tangerine project have a thickness of ~50 µm with an approximately 10 µm thick epitaxial layer. Three different sensor layouts are available, with different doping profiles affecting charge collection, the so-called *standard* [33], *n-blanket* [16] and *n-gap* [17] layouts. The three layouts are displayed on the top of Figure 4.1. In the sketch, the p-wells hosting the electronics are in the upper corners. Between them, the small n-type collection electrode is indicated. The high doped p-substrate (~40 µm) extends from the bottom of the epitaxial layer to the backside of the sensor.

The standard layout is similar to the one present in the ALPIDE sensor that is currently installed in the ALICE Inner Tracking System [18]. The depletion region starts growing from the pn junction around the n-type collection electrode. Only a small region gets depleted, resulting in large diffusion of charge carriers outside this region, high charge sharing, and slow charge

collection. Consequently, the standard layout has a better spatial resolution, but a lower efficiency, compared to the other layouts.

The n-blanket layout introduces a deep low dose n-type implant layer. Pn junctions are now formed around the p-well and between the n-implant and the p-epitaxial layer, increasing the depletion region through the epitaxial layer, where charges are collecting faster via drift. The charge sharing and spatial resolution are deteriorated with respect to the standard layout, but the efficiency increases.

The n-gap layout has a gap in the n-type layer compared to the n-blanket layout. This gap creates vertical pn junctions, increasing the lateral component of the electric field. Charge carriers are pushed faster towards the collection electrode, and the efficiency, time resolution, and radiation tolerance are improved [17]. However, the charge sharing between neighbouring pixels is reduced, deteriorating the resolution.

As a consequence, a compromise has to be made between efficiency and spatial resolution. These observables can be visualized in the Monte Carlo simulations with Allpix^2 using imported fields from TCAD. The second row of Figure 4.1 shows line graphs, i.e. the trajectories followed by the collected electrons. Most of the charges created in the high-doped substrate recombine with the silicon lattice. Differences in drift and diffusion can be seen. While for the standard layout, the collection of charges in the epitaxial layer (top $\sim$10 µm) is done via diffusion, in the n-blanket and n-layer charges are mostly collected via drift, and the trajectory of the collected electrons in the epitaxial layer can be seen to be more linear. The three layouts have the same substrate; diffusion dominates there, and the line graphs of the three layouts are similar.

The in-pixel cluster size comparison is shown in the third row of Figure 4.1. The collection electrode is in the center. Around it, for all the layouts, the cluster size is one. The diffusion of charge carriers in the corners of the standard and n-blanket layout results in cluster size four, while the n-gap has cluster size one in almost the entire pixel cell.

In the last row of Figure 4.1, the in-pixel efficiency is shown. The efficiency deteriorates as a function of the distance to the collection electrode due to charge sharing. This is reflected in the low efficiency in the corners of the standard layout, while the n-gap layout is still highly efficient in this region.

As a summary, Figure 4.2 shows a simulation of the spatial resolution in x (similar in y) and Figure 4.3 the efficiency as a function of the detection threshold for the three layouts. By increasing the threshold, both observables deteriorate. The n-gap layout has a more moderate degradation of the resolution and maintains high efficiency even at higher thresholds. On the contrary, the efficiency of the standard layout deteriorates faster but still has a good resolution at higher thresholds.

As shown in Figure 3.4, the in-pixel efficiency mainly deteriorates in the edges and corners

for higher thresholds, and the pixel is only efficient in a small region around the collection electrode. Outside of this small region, the combination of large cluster sizes and high detection thresholds results in undetected particles that do not contribute to the spatial resolution calculation. Consequently, the charge-weighed cluster reconstruction is applied to a small fraction of events, and the residual width is smaller. This effect is visible in Figure 4.2 at about 300 electrons when a plateau is reached in the resolution for the three layouts.

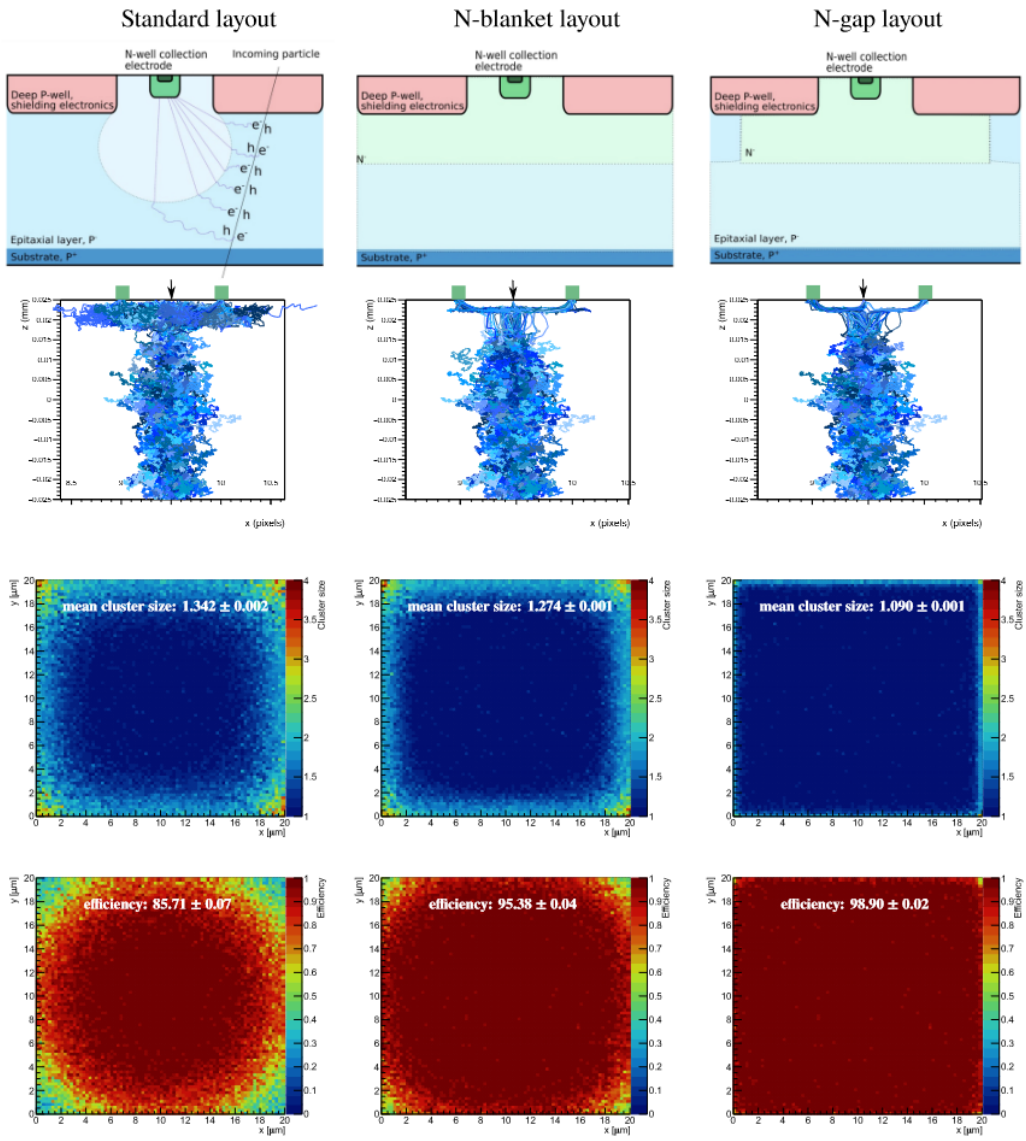

Figure 4.1: On the top, a sketch of the three sensor layouts: standard (left) [33], n-blanket (middle) [16] and n-gap (right) [17]. On the second row, the corresponding line graphs. The vertical axis shows the sensor depth and the x-axis uses "pixel pitches" as units (the collection electrodes are indicated in green at integer number positions). A single 5 GeV electron-event is shot approximately in the center between the 9^{th}- and 10^{th}- pixel. The exact incident position is marked with a black arrow. On the third and fourth rows, their corresponding in-pixel cluster size and efficiency. Simulations obtained with Allpix^2 for a pixel pitch of 20 µm and a detection threshold of 200 electrons.

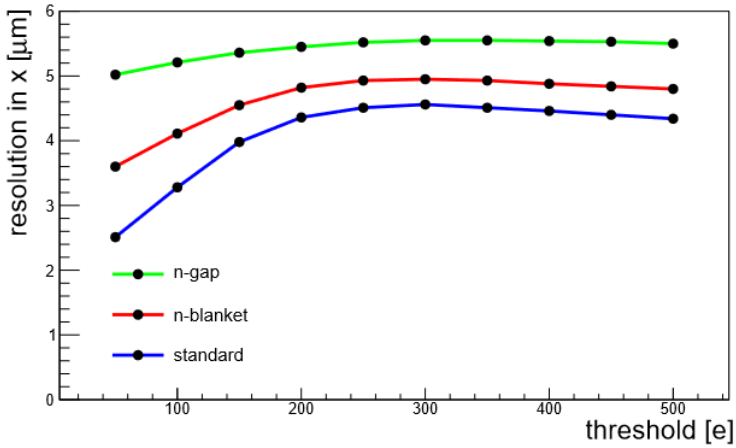

Figure 4.2: Spatial resolution in X for different detection thresholds. Simulations obtained with Allpix^2 for a pixel pitch of 20×20 µm.

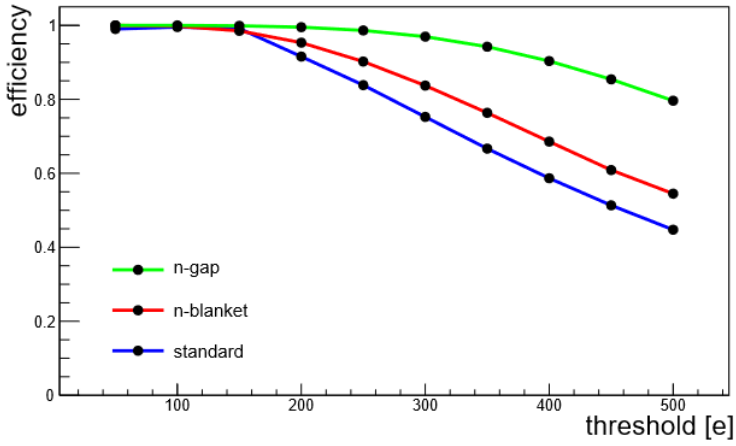

Figure 4.3: Efficiency for different detection thresholds. Simulations obtained with Allpix^2 for a pixel pitch of 20×20 µm.

CHAPTER 5

Simulation Validation Studies with Allpix^2

In order to have accurate and optimized Monte Carlo simulations of the investigated sensors, several studies are carried out. The parameters described in Section 2 in the different stages of the Allpix^2 simulation are varied, in an effort to find optimal values in terms of accuracy and simulation performance. This examination allows having a better understanding of the sensor behavior, and of the simulations. Taking into account the accuracy of the physics described, the duration and the memory footprint of the simulations, the parameters are fixed for further studies, including the beam telescope simulations described in Chapter 7. This chapter summarizes these simulation optimization studies for the sensors being developed in the Tangerine Project. Similar studies for other sensor types could lead to very different results.

Unless specified otherwise, all the results presented in this chapter are obtained with the standard layout with a pixel size of 20 µm and with a detection threshold of 100 electrons. 250 000 single-electron events are simulated for each tested parameter value.

5.1 Electric field and doping profile initialization

Number of divisions in TCAD-to-Allpix^2 conversion

Figure 5.1 shows the meshing used in a TCAD simulation. The 3D meshing is done in tetrahedra. It is dependent on doping concentration gradient, with a finer mesh in the non-uniform regions (the boundary between two differently doped regions). The calculation of the quasistationary simulation is performed in the vertices of the mesh. The vertex coordinates and values of the electric field and doping profiles in those vertices are imported into Allpix^2. This mesh adaptation process is done by the `Mesh Converter` module in Allpix^2. Using the method of barycentric interpolation, the fields are adapted to a regularly spaced grid [2] for faster field value lookup during simulation. The number of divisions selected for the mesh is related to the granularity of the field in Allpix^2. Different mesh divisions of the same imported field are tested to study their influence on spatial resolution and efficiency. The results are summarized in Table 5.1.

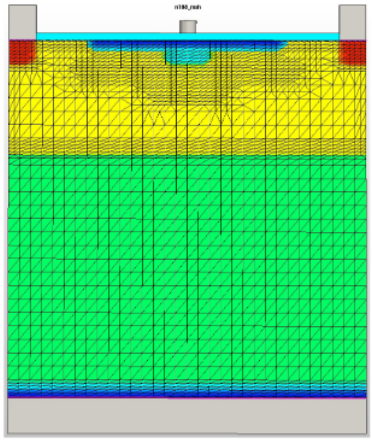

Figure 5.1: TCAD finite-element mesh in 2D with the collection electrodes in the corners. The mesh granularity is adapted to the different regions. From [20].

Table 5.1: Cluster size in X, spatial resolution in X and efficiency for different mesh divisions selected in Allpix^2 for the same TCAD field. In the top block, the number of divisions in the z-axis is altered. In the block in the center, the number of divisions in the z-direction is fixed to 100, while different mesh divisions in the x- and y-axis are tested. The third block shows a highly granular mesh, and the bottom block corresponds to a coarse mesh in the three dimensions. Uncertainly is only statistical.

Mesh divisions	Cluster size in X	Resolution in X [µm]	Efficiency [%]
100×100×100	1.42 ± 0.01	3.29 ± 0.01	99.58 ± 0.02
100×100×50	1.43 ± 0.01	3.31 ± 0.01	99.72 ± 0.02
100×100×10	1.45 ± 0.01	3.33 ± 0.01	99.78 ± 0.02
300×300×100	1.43 ± 0.01	3.28 ± 0.01	99.58 ± 0.02
100×100× 100	1.43 ± 0.01	3.29 ± 0.01	99.58 ± 0.02
50×50×100	1.43 ± 0.01	3.29 ± 0.01	99.56 ± 0.02
20×20×100	1.43 ± 0.01	3.30 ± 0.01	99.58 ± 0.02
20×20×10	1.41 ± 0.01	3.41 ± 0.01	99.70 ± 0.02
500×500×300	1.42 ± 0.01	3.30 ± 0.01	99.60 ± 0.02

The first block of Table 5.1 reflects variations in the mesh size along the sensor depth (z-axis). By decreasing the granularity in the sensor depth, the small region with high a electric field around the collection electrode is spread out (see Figure 5.2), and the spatial resolution deteriorates. The same effect can be observed in the second block of Table 5.1 where the mesh divisions in the x-y axis are varied. However, the effect is significantly smaller. This is due to the fact that in the standard layout the charge carriers collected via drift travel mainly vertically, and thus, the mesh granularity in the z-axis is the most important parameter. This situation might be different in the n-blanket and n-gap layouts where the lateral component of the electric field favors the

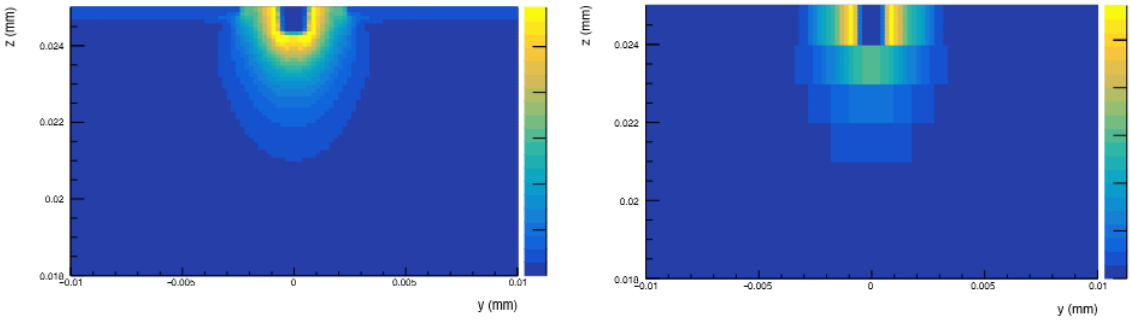

Figure 5.2: Electric field map in Allpix^2 for two different mesh divisions: 100×100×100 on the left and 100×100×10 on the right. The color scale indicates the strength of the field and has the same scale in both plots.

collection of charge carriers via drift far from the collection electrodes. The third block of the table shows a coarse mesh in the three dimensions, where the resolution is further deteriorated. An extremely fine mesh in which the TCAD granularity is exceeded is shown in the fourth block. In this case, the memory footprint of the simulations is notably increased, while the resolution and efficiency do not show a significant change in comparison with other mesh granularities.

Conclusion: Changes along the z-axis have a larger effect than changes in x and y for the standard layout. Differences in mean cluster size, spatial resolution and efficiency are understood and attributed to the different magnitudes of the electric field within the mesh divisions. Having a finer mesh does not slow down the simulations, although it increases the memory footprint. In the following, 300×300×100 divisions, corresponding to 15×15×30 bins per micrometer, will be used.

5.2 Energy deposition

GEANT4 Physics list

The main goal of this study is to see if there are significant differences between GEANT4 physics lists. Thus, different GEANT4 physics lists are tested. Some of them slow down the sensor simulations, or even break off the full telescope simulation due to problems with aborted events with a negative local time and long negative step lengths. The latter is the case of the standard physics list `QGSP_BERT`. Furthermore, particle physics list like `FTFP_BERT_LIV` are `FTFP_BERT_EMV` are fast and lead to similar results.

Conclusion: `FTFP_BERT_LIV` is used in the following, in agreement with the recommendation given by GEANT4 for tracking applications [34].

Maximum length of a simulation step

The maximum length of a simulation step in the sensitive volume is studied. This parameter only concerns the initial deposition energy, and does not influence the charge carrier propagation.

Only the maximum length can be defined in GEANT4, and not the real one as it is automatically chosen by GEANT4. Figure 5.3 shows the distance between charge depositions for a simulation with the maximum step length equal to 1 µm (default value) for three different sensor thicknesses. For all of them, most of the charge depositions occur a step lengths equal to the chosen maximum step length. However, in some steps, there is no charge deposition, and the distance between charge deposition increases. This can be seen in the peaks at integer numbers. Moreover, a few charges are deposited at random step lengths shorter than the maximum.

Although the duration of the simulations (for the investigated sensors) is not influenced by this parameter, the cluster size, and thus the position resolution, are. Figure 5.4 shows the cluster size in X and the total charge collected per event for different maximum step lengths. Up to 5 µm maximum step length, there is no significant difference in these observables. Higher values deposited charges only in a few regions of the sensor. In the case of the 25 µm maximum step length, charges are deposited only around two regions: close to the collection electrode and in the substrate. Most charges deposited in the substrate recombine, and the ones deposited close to the collection electrode drift and are collected quickly. This results in more events with cluster size one, and a shift to the left in the peak of the Landau distribution.

Conclusion: As the duration of the simulations is not affected by the maximum length of a simulation step in the deposition stage with GEANT4, and having not observed significant differences among small values, the default value of 1 µm is chosen for use in the simulations.

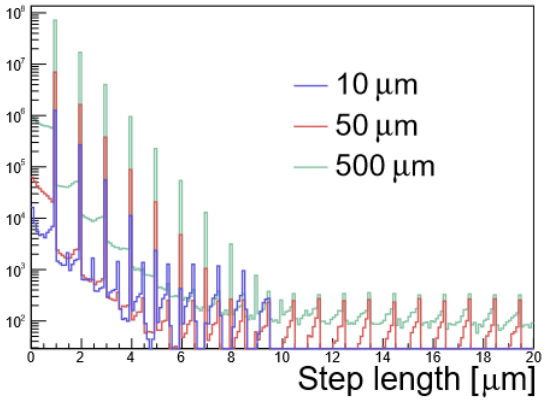

Figure 5.3: Step length distribution for different sensor thicknesses.

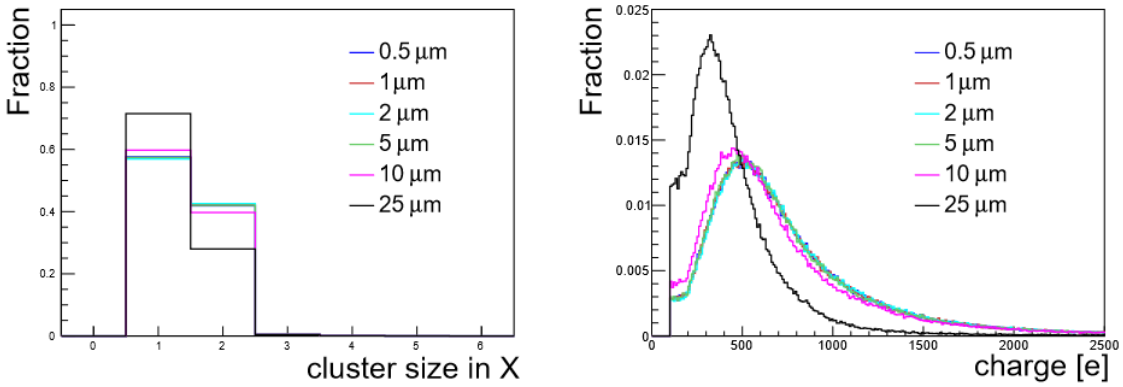

Figure 5.4: Cluster size in X (left) and total charge collected per event (right) distributions for different maximum lengths of a simulation step.

Photoabsoption Ionization Model

The effect on the photoabsorption ionization model (PAI) is studied for different sensor thicknesses. Figure 5.5 compares the total charge deposited in 10, 50 and 500 µm thick silicon sensor. For larger sensor thickness, there is no significant difference between simulations with and without PAI model. However, for the 10 µm thick sensor, the difference is noticeable.

Conclusion: Although the duration of the simulations is slightly increased when the PAI model is activated, in thin sensors like the ones studied in this thesis, ionization via photoabsorption is significant, and thus, this model needs to be enabled in the simulations.

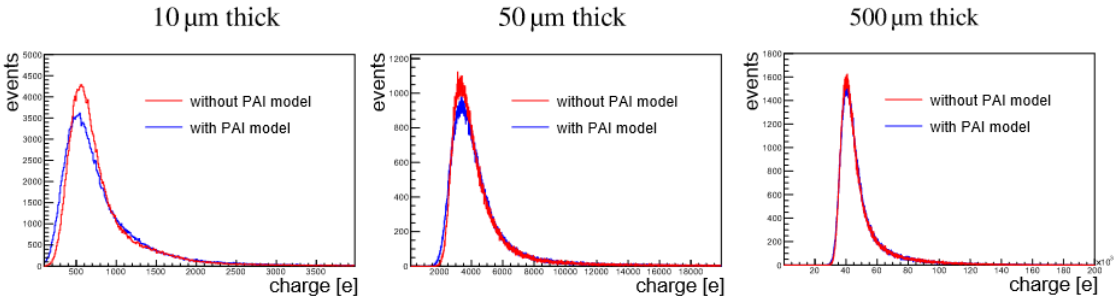

Figure 5.5: Charge generated by deposited energy (in electrons) for a 5 GeV single-electron beam in 10 µm (left), 50 µm (middle) and 500 µm (right) of silicon. The simulations are shown with the PAI model enabled and disabled.

5.3 Charge propagation

The `GenericPropagation` module takes the largest amount of time ($\sim 90\,\%$) and it is one of the most important steps in the simulation. Therefore, validation and optimization of the parameters are fundamental. In addition to the parameters that will be discussed below, electron/hole mobilities and recombination have also been studied in the Tangerine group [35]. The mobility and recombination models used are the Masetti-Canali and SRH-Auger respectively, due to their dependence on the doping concentrations.

Maximum number of charge carriers propagated per step

Charge carriers from the same deposition point can be propagated together, treated as a single particle to speed up the simulations. Table 5.2 shows that the maximum number of charge carriers propagated together as a group per step influences the duration of the simulations. It is shown that this dependence is nearly linear. Figure 5.6 compares the cluster size in X and the total charge collected per event distributions for the different group sizes. It can be seen that there is no considerable difference between groups of up to 1,5, or 10 charge carriers propagated together. However, bigger groups of charge carriers propagated together have larger cluster sizes because of their higher probability to overcome the detection threshold (leading to the deterioration of the spatial resolution - in reality not all the charges in a group would have traveled to the same collection electrode). For the same reason, the peak of the Landau distribution is shifted to higher values.

Table 5.2: Duration of the simulations, resolution in X and efficiency for different group size of charge carriers propagated together in one step.

Maximum number of charge carriers propagated per step	Duration of the simulations	Resolution in X [µm]	Efficiency [%]
1	1 920 ms/event per worker	3.57 ± 0.01	98.91 ± 0.02
5	400 ms/event per worker	3.59 ± 0.01	98.91 ± 0.02
10	240 ms/event per worker	3.65 ± 0.01	98.89 ± 0.02
25	80 ms/event per worker	3.76 ± 0.01	98.90 ± 0.03
50	80 ms/event per worker	3.95 ± 0.01	98.80 ± 0.02

Table 5.2 also summarizes the spatial resolution in X and efficiency for the different group sizes. On the one hand, the efficiency is practically independent of the group size. As a consequence, if only sensor efficiency studies are desired, the maximum number of charge carriers propagated per step can be increased. However, the same is not true for the spatial resolution. The spatial resolution starts deteriorating considerably for larger groups, as explained above. Thus, for spatial resolution studies, the group size should be as small as possible. The difference between groups of 1 or 5 charge carriers is minimal, but the time of the simulation is almost a factor of five longer.

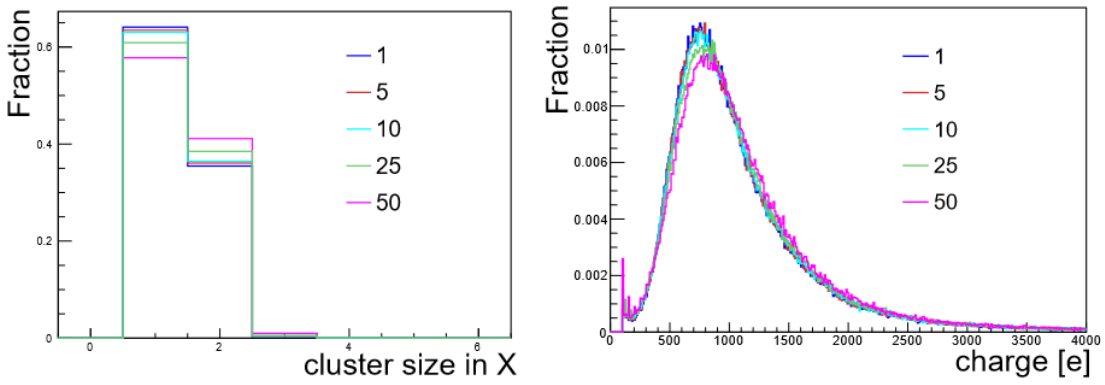

Figure 5.6: Cluster size in X (left) and total charge collected per event (right) for different maximum numbers of charge carriers propagated together. The simulations are performed with the electronics noise equal to zero, and the maximum length of a simulation step in the deposition stage with GEANT4 equal to 1 µm.

Conclusion: The number of charge carriers propagated together directly impact the duration of the simulations. Further, it has a small impact on the efficiency, but a significant impact on the resolution. In the following, the maximum number of charge carriers propagated per step is fixed to five, having not observed any notable difference for smaller values.

5.4 Charge transfer

Collection implant size

In TCAD, the implant size is defined by the difference in doping concentrations, with some diffusion between them. In Allpix^2, however, it is necessary to explicitly define it as a parameter in size (a square in x and y) and in depth (in z). Only the charge carriers within the implant region in Allpix^2 are collected, and outside this region, they are ignored and lost. Figure 5.7 shows the resolution in X, efficiency, cluster size X and mean cluster charge collected per event for different implant sizes in X (same in Y) defined in Allpix^2. For implant sizes below 1.5 µm, not all the charges that should be collected after the integration time are collected, resulting in lower cluster sizes, lower efficiency, and worse resolution. The reason is that the imported field from TCAD has a larger implant size where the field is nearly zero. Once the charge carriers arrive at the collection electrode defined by TCAD, they are mostly immobile and they have a small probability to reach the small implant defined in Allpix^2. Thus, charge carriers are lost in the final diffusion steps, as sketched in Figure 5.8.

The implant depth can be also modified in Allpix^2, but since diffusion is not the dominant movement of charge carriers along the z-axis close to the collection electrode, the difference is negligible.

Conclusion: The collection electrode size in Allpix^2 has a significant impact on the observable studied. A size at least as big as the TCAD implant size is needed. For further studies, this collection electrode size is fixed to 2.2×2.2×0.6 µm^3 in Allpix^2.

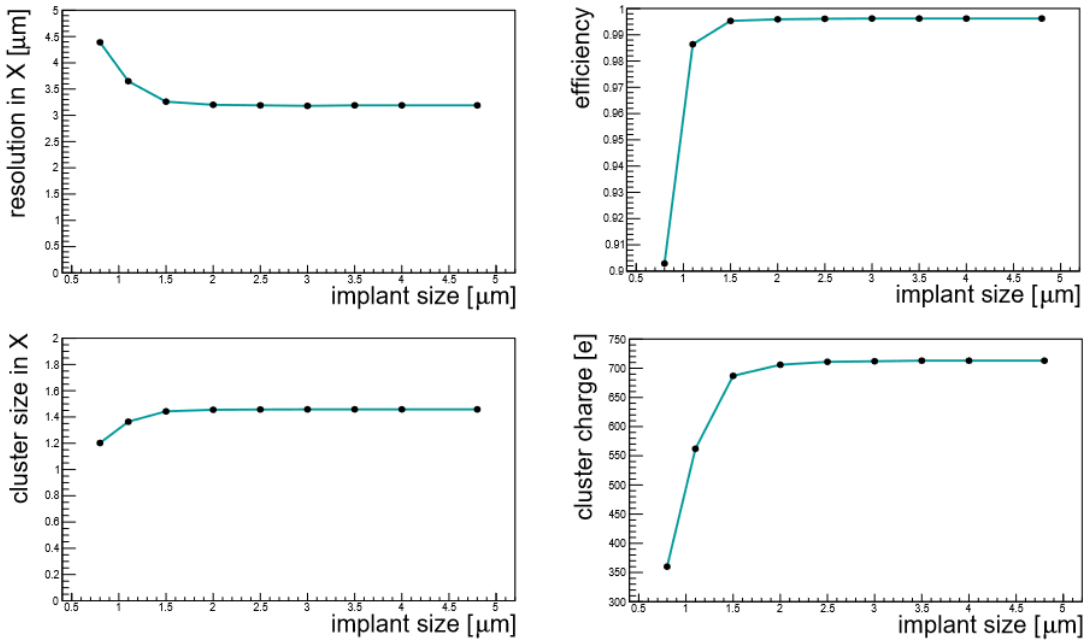

Figure 5.7: Resolution in X, efficiency, cluster size in X and mean cluster charge collected per event as function of the implant size in X and Y).

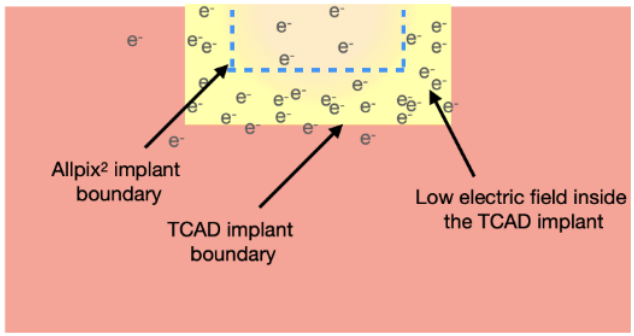

Figure 5.8: Sketch of a small implant size in Allpix^2 in comparison to the TCAD implant. The electrons follow the field lines defined by TCAD and once the arrive to the collection electrode, they do not move due to the high doping concentration and no field.

5.5 Conclusion

Validation studies of the simulations with the investigated sensors have been performed. The module parameters in Allpix^2 have been tested in order to determine if they are stable or have a significant influence on the results. This has been done for all the stages in the simulations. Consequently, the values of the parameters have been chosen for the following studies described in this work.

CHAPTER 6

High Occupancy Studies

6.1 Introduction

In many particle physics experiments the same pixel can be hit by two or more particles in a single event. This is, for example, the case of the LUXE experiment (Laser Und XFEL Experiment), a new experiment proposed at DESY and the European XFEL [36]. In the LUXE experiment two type of collisions will be studied: electron-laser ($e^- + n\gamma_L \rightarrow e^- + \gamma$) and gamma-laser ($\gamma + n\gamma_L \rightarrow e^- + e^+$). For the gamma-laser mode, positrons and electrons will be detected with a tracker consisting of ALPIDE sensors [37]. However, for the electron-laser mode, due to the high rates of emitted electrons (up to 10^9 particles per bunch crossing), the ALPIDE sensors are not suitable, and gas Cherenkov detectors and a scintillation screen will be used to reconstruct the electrons trajectory. Motivated by this kind of scenario, the detection capabilities of the Tangerine project sensors in high occupancy situations have been studied.

6.2 Analysis

Two-particle events deposit a higher amount of charge in the sensor than one-particle events. This can be observed in the distribution of the total charge collected per event. Differences could be also observed in the cluster size distributions, especially for particles traversing the pixel cell close to the edges and corners where two-particle events will have a higher chance to be detected than one-particle events. Therefore, the initial goal is to differentiate one- and two-particle events by setting a cut in the cluster size and total charge collected per event distribution. To do so, different scenarios are simulated, in which one- or two-particle events hit the same pixel cell at different positions. Once these particular cases are understood, in the next step, a more realistic scenario with one- and two-particle events uniformly distributed in a pixel is simulated.

6.2.1 Particular cases

The following particular cases are studied: one- and two-particle events hitting in the center of the pixel cell (situation 1), in two parallel edges of a pixel cell (situation 2), in opposite corners (situation 3), one-particle events in the center and two-particle events in one edge (situation 4)

and one-particle events in the one edge and two-particle events in the center. These situations are represented on the left side of Figure 6.1.

The charge deposition module in Allpix^2, `[DepositionGeant4]` allows to use GEANT4 macros. The macro is highly configurable and allows for the deposition of charges in two separate positions at the same time. An example of a GEANT4 macro with two-particle events hitting two parallel edges of the same pixel cell is given below.

```
# Source 1
/gps/particle e-
/gps/pos/type Point
/gps/pos/centre 0.01 0 -10 mm
/gps/ene/mono 5 GeV
/gps/direction 0 0 1
/gps/intensity 1
# Source 2, in a different position
/gps/source/add 1
/gps/particle e-
/gps/pos/type Point
/gps/pos/centre 0.01 0.02 -10 mm
/gps/ene/mono 5 GeV
/gps/direction 0 0 1
/gps/source/multiplevertex 1
```

An example of configuration module to load the macro with the parameters decribed in Chapter 2 is:

```
[DepositionGeant4]
physics_list = FTFP_BERT_LIV
source_type = "macro"
file_name = "twoElectronSource.mac"
max_step_length = 1um
enable_pai = true
```

Figure 6.1 shows the cluster size in X, cluster size in Y, and total charge collected per event distribution for the five situations under study. While in some situations, one- and two-particle events can be distinguished with the cluster size projections, in others it is necessary to include the information enclosed in the charge distributions. The latter is the case of situation 1, and more in general, for any event with cluster size one in X and Y, which is the most dominant cluster size for particles hitting around the pixel center with a typical detection threshold (see Figure 4.1).

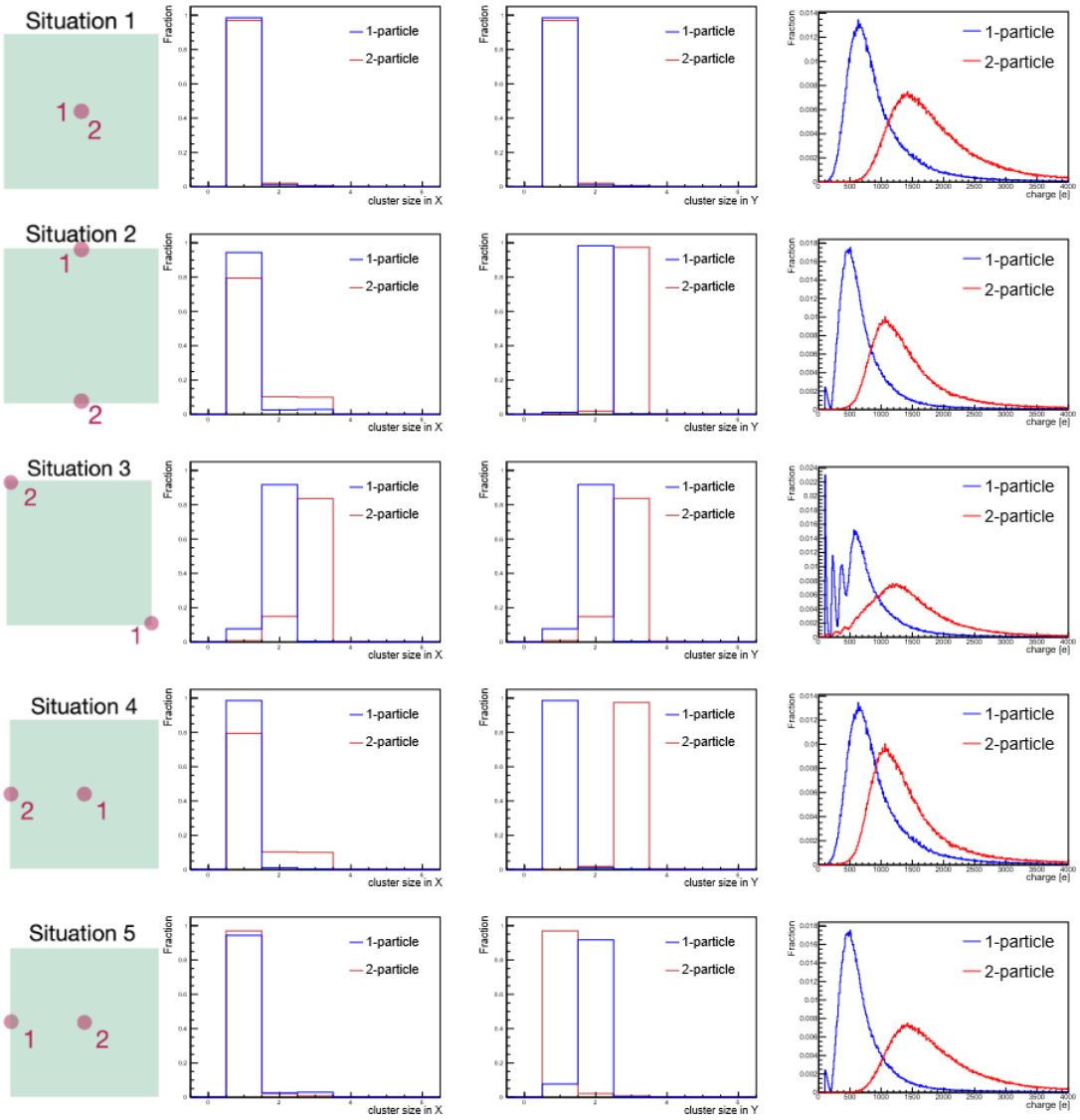

Figure 6.1: On the left, a sketch of the five particular cases simulated, the numbers in red indicates how many particles are deposited in each position. On the right, their corresponding cluster size and X and Y distributions, and the total charge collected per event distribution for one- and two-particle events. Simulations are performed using the standard layout with a pixel pitch of 20 µm and a detection threshold of 100 electrons. The discrete peaks at integer values of the detection threshold in situations 2, 3 and 5 is a consequence of the detection threshold in large charge sharing situations.

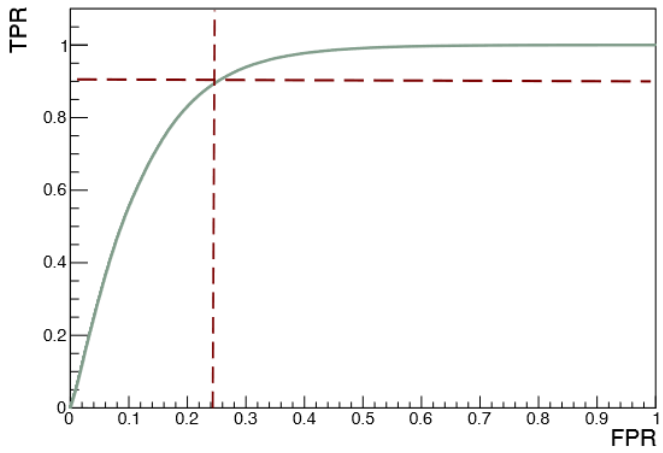

Figure 6.2: ROC curve for each possible cut-off value (in electrons) in the distribution of the total charge collected per event in situation 1, giving rise to different TPR and FPR. The red lines indicate the values of TPR and FPR where TPR−FPR is maximized. Study done with the standard layout with a pixel pitch of 20 µm and a detection threshold of 100 electrons.

Two-particle events generate more charge carriers than one-particle events. However, due to the long tail of the Landau distribution, the collected charge distributions overlap in a large range. In order to define the best cut that separates both types of events, a study of the ROC (Receiver Operating Characteristic) curve is performed.

The ROC curve computes for each possible cut the True Positive Rate (TPR: the probability that two-particle events are correctly classified as two-particle events) and the False Positive Rate (FPR: the probability that one-particle events are incorrectly classified as two-particle events). The point where the difference between TPR and FPR is maximized defines the optimal cut in the charge collected per event distribution. This is illustrated for Situation 1 in Figure 6.2. The optimal cut is at about 1 100 electrons. For situation 1, above this value, events are classified as two-particle events, and below as one-particle events. The same is done for all the situations.

Assuming that is it equally severe for an experiment to classify one-particle events as two-particle events and two-particle events as one-particle events, the misclassification rate (MR) can be calculated from the wrongly classified events when such a cut is applied. Table 6.1 summarizes the defined optimal cuts and the corresponding misclassification rates. For situation 1, the confusion matrix can be read as follows:

- In ∼90 % of predictions, two-particle events are correctly predicted as two-particle events (TP: True Positive).
- In ∼75 % of the predictions, one-particle events are correctly predicted as one-particle events (TN: True Negative).
- In ∼10 % of the predictions, two-particle events are incorrectly predicted as one-particle

events (FN: False Negative).
- In ~25 % of the predictions, one-particle events are incorrectly predicted as two-particle events (FP: False Positive).
- ~18 % of the predictions are incorrectly classified (MR: misclassification rate, calculated as MR = (FP+FN)/(TP+TN+FP+FN)).

Table 6.1: Confusion matrices with the optimal cuts in the total charge per event collected distribution, obtained from the ROC curves, and the misclassification rate for the five situations shown in Figure 6.1.

		Situation 1		Situation 2		Situation 3	
		Actual		Actual		Actual	
		2 particles	1 particle	2 particles	1 particle	2 particles	1 particle
Predicted	2 particles	TP:0.9008	FP:0.2527	TP:0.8980	FP:0.2519	TP:0.7997	FP:0.2486
	1 particle	FN:0.0992	TN:0.7473	FN:0.1020	TN:0.7481	FN:0.2003	TN:0.7514
Optimal cut		1 109 electrons		837 electrons		938 electrons	
MR		18 %		18 %		22 %	

		Situation 4		Situation 5	
		Actual		Actual	
		2 particles	1 particle	2 particles	1 particle
Predicted	2 particles	TP:0.9216	FP:0.1974	TP:0.8815	FP:0.3131
	1 particle	FN:0.0784	TN:0.8026	FN:0.1185	TN:0.6869
Optimal cut		934 electrons		1 004 electrons	
MR		13 %		21 %	

Misclassification rates above 20 % are obtained for situations 3 and 5. However, this result may be further improved including the cluster size information. Hence, a multivariable analysis might refine the decision cuts.

6.2.2 Uniform distributed beam

In real experiments, the flux of particles is different for each direction, in a small section like a pixel cell, the probability to hit any part of the pixel can be considered to be uniform. Therefore, one and two-particle events are simulated uniformly distributed in a pixel cell to extend the studies of high occupancy situations. One way to simulate a uniform distributed single-electron beam over the pixel cell with GEANT4 in Allpix^2 is given below.

```
[DepositionGeant4]
physics_list = FTFP_BERT_LIV
number_of_particles = 1
particle_type = "e-"
source_energy = 5GeV
source_type = "square"
source_position = 10um 10um -10mm
square_side = 20um
square_angle = 0deg
max_step_length = 1um
enable_pai = true
```

Due to the uniform distribution over a square pixel, the cluster size in X and Y are identical. Figure 6.3 shows the cluster size in X and the total charge collected per event for one- and two-particle events for the three layouts. As expected from Chapter 4, the standard layout has larger cluster sizes and smaller charge collection in comparison with the n-blanket and n-gap layouts. Furthermore, two-particle events have larger cluster sizes and charge collection than one-particle events, although they overlap in a large region.

The same study as before with the ROC curves is done to find the optimal cut to separate one- from two-particle events according to the total charge collected per event distributions. Table 6.2 summarises the rates and optimal cuts. Since the charge collection efficiency for the n-blanket and n-gap layouts are higher than for the standard layout, the optimal cut in electrons is shifted to higher values, and this slightly improves the misclassification rate. A misclassification rate of 19 % is calculated for the standard layout and of 18 % for the n-blanket and n-gap layouts.

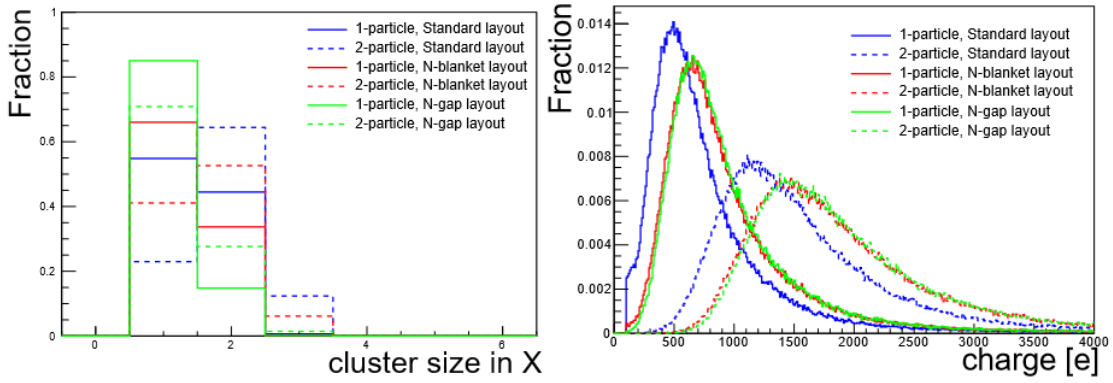

Figure 6.3: Cluster size in X (left) and collected charge per event (right) distributions created by 1-particle and 2-particle uniform distributed events in the standard, n-blanket and n-gap layouts

Table 6.2: Confusion matrices with the optimal cuts in the total charge per event collected distribution, obtained from the ROC curves, and the misclassification rate (MR) for the standard (left), n-blanket (middle), and n-gap (right) layouts.

		Standard layout		N-blanket layout		N-gap layout	
		Actual		Actual		Actual	
		2 particles	1 particle	2 particles	1 particle	2 particles	1 particle
Predicted	2 particles	TP:0.8734	FP:0.2654	TP:0.8940	TP:0.2607	TP:0.9016	TP:0.2599
	1 particle	TP:0.1266	FN:0.6346	TN:0.1060	TP:0.7393	TP:0.0989	TP:0.7405
Optimal cut		896 electrons		1 108 electrons		1 127 electrons	
MR		19 %		18 %		18 %	

In contrast to the previous situations, in which the cluster size distribution could lead to the correct classification, now the cut is not trivial and a multivariable analysis is needed. A multivariable analysis using a Boosted Decision Tree [38] with the cluster size in X and Y and the total charge collected per event as variables is carried out. The study is done with the standard layout, using the TMVA library provided by ROOT [39]. The first decision cut obtained is applied to the total charge collected per event distribution, corresponding to 847 electrons. Although ROOT also bases the decision of the cut-off value in a ROC curve study, the obtained value is smaller than the one calculated above. The reason for this difference is that in the dataset provided to ROOT, events with zero charge are included (to achieve a more realistic scenario), and thus biasing the cut to lower charge values. To reduce the FP rate, an extra cut is applied at 1 090 electrons. However, the TP rate for events fulfilling both conditions is very low. To enhance the performance, combinations of the variables are also included. This results in the cut $clusterSizeX + clusterSizeY > 3$. The tree structure with the rates is represented in Figure 6.4.

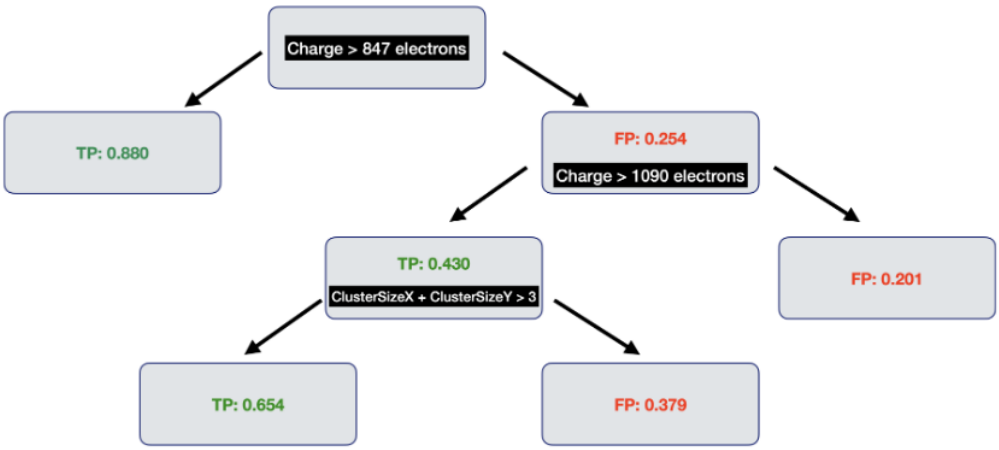

Figure 6.4: Boosted decision tree structure.

6.3 Conclusion

The performance of the sensor in high density situations is being studied. Using only the cluster size and the total charge collected per event distributions, one- and two-particle events can be distinguished with a misclassification rate of approximately 20 %. The n-blanket and n-gap layouts show better performance in this situation. The first attempt at using multivariable analysis did not provide significantly better results. However, further studies including more variables and more sophisticated techniques could enhance the obtained results.

CHAPTER 7

Beam Telescope Simulations

Once the sensor simulations have been validated and the optimal parameters have been determined, a more complex system can be simulated with Allpix^2. In this work, a beam telescope is simulated, in which the investigated sensors are arranged into planes and the tracking performance is calculated.

The sensors simulated have a pixel size of $20 \times 20\,\mu m^2$. Six parallel telescope planes are created, each with a matrix of $1\,024 \times 1\,024$ pixels. To study the telescope resolution at the DUT position, a silicon box with a thickness of 50 µm is placed in the center, at which the Monte Carlo truth position of the simulated particle can be compared with the reconstructed track intercept. A beam of 5 GeV electrons with a Gaussian profile is simulated, crossing the setup in the z-direction, perpendicular to the sensor planes (see Figure 3.1). For each telescope geometry presented, 250 000 single-electron events are simulated, meaning that the statistical uncertainties are very small (error bars are smaller than the dot size in all the plots presented here). Random misalignment of the reference planes (in position and orientation) is introduced.

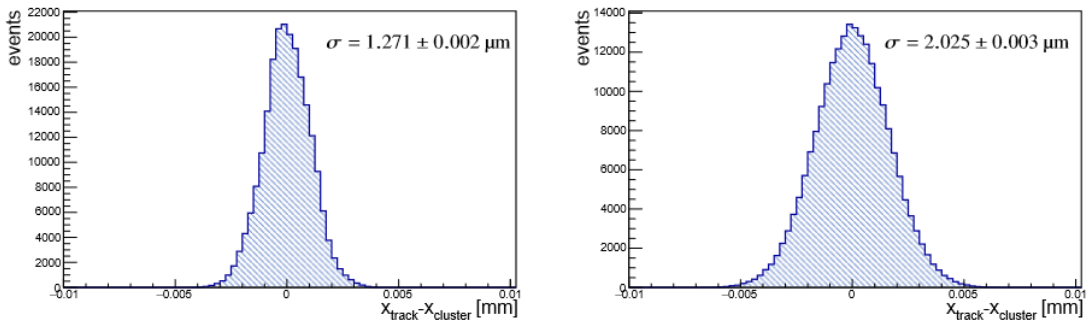

Figure 7.1: Residual distribution in x between the track intercept and the center-of-gravity position of the associated cluster for the first (left) and third (right) telescope planes.

7.1 Track reconstruction and residuals

The trajectory of the incoming relativistic particle through the telescope plane is reconstructed as explained in Chapter 3 using GBL. For each event, the following information is available: the Monte Carlo truth, the reconstructed center-of-gravity position of the clusters in the telescope planes, and the reconstructed track intercepts at all planes.

By computing the difference between the track intercept and the associated cluster center for a set of tracks, the biased residual distributions in x and y with respect to the telescope plane are obtained. Figure 7.1 shows the residual distributions for the first and third telescope planes in the x (similar in the y) direction. The standard deviation of the central 99.73 % of those distributions defines the biased residual width.

The telescope resolution at the DUT position is obtained from the residual distribution width between the Monte Carlo truth position and the track intercept with the DUT (excluded in track reconstruction). In this way, the telescope resolution at the DUT position is independent of the intrinsic resolution of the DUT.

7.2 Telescope resolution

Figure 7.2(a) shows the telescope resolution at the different planes separated by a distance dz of 150 mm. The red curve represents the biased residual width between the cluster centers and the associated Monte Carlo truth positions, i.e, the intrinsic resolution of the sensors. In blue, the biased residual width between the cluster center and the track intercept on the planes is shown. It

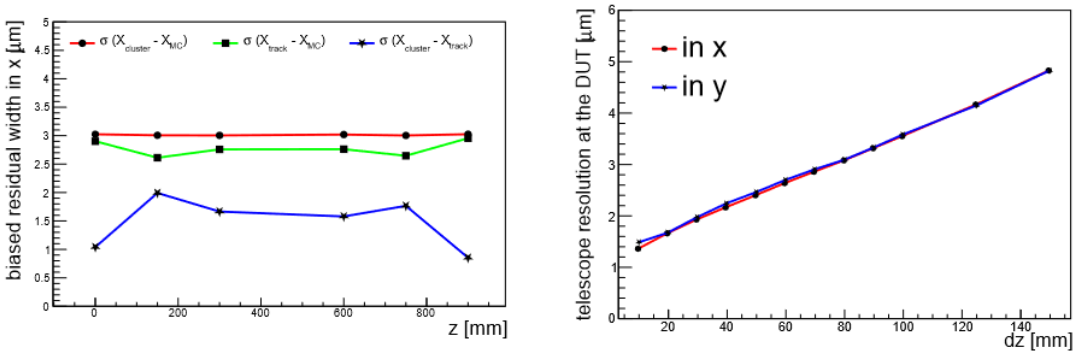

(a) (b)

Figure 7.2: (a) Biased residual widths between the cluster center and the Monte Carlo position, track intercept and Monte Carlo position, and cluster center and track intercept for each of the telescope planes at a distance of dz = 150 mm. (b) Telescope resolution at the DUT position for different distances between telescope planes.

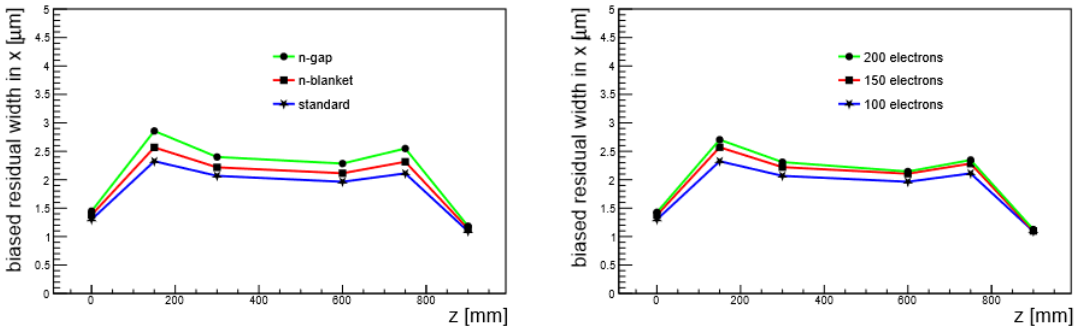

(a) (b)

Figure 7.3: (a) Biased residual widths for the three different pixel layouts for the six telescope planes. Simulations performed with a threshold of 100 electrons and a pixel pitch of 20 µm. (b) Biased residual widths for the six telescope planes with three different detection thresholds. Simulations performed with the standard layout with a pixel pitch of 20 µm.

can be seen that the telescope resolution slightly deteriorates from the DUT towards the second and fifth telescope planes (the residuals get larger). The small biased residuals in the first and last beam telescope planes are a consequence of the GBL track reconstruction algorithm: for the outermost planes, there is no next measurement to constrain the track, so the algorithm only minimizes the distance between the track and cluster positions, and the residuals get smaller. For the same reason, the biased residual widths between the track intercept and the Monte Carlo position (in green) converge in the outermost planes to the intrinsic resolution of the sensors. Since the cluster center is used for tracking, and not the Monte Carlo truth position, the distance between the track intersect and the cluster center is in general smaller than the separation between the Monte Carlo position and the track intercept, resulting in smaller residuals. Moreover, an asymmetry in the difference between the cluster center and the track intercept the for the upstream and downstream planes can be observed. The origin of this asymmetry is being investigated.

The telescope resolution in x and y at the DUT position is shown in Figure 7.2(b) for different distances between telescope planes dz. The telescope resolution improves linearly when this separation is reduced. The fact that the projections in x and y are not perfectly overlapping is an effect of the remaining misalignment of the planes after the alignment procedure.

Figure 7.3(a) shows the biased residual widths between the cluster center and the track intercept for the three different sensor layouts, and for the six telescope planes with dz of 150 mm. As expected from an improvement of the charge-weighted cluster center reconstruction for cluster sizes larger than one, the standard layout has the best tracking resolution (see Chapter 4). However, this layout is expected to have the lowest efficiency of the three layouts. Less charge sharing is achieved in the n-blanket and n-gap layouts, resulting in worse position resolution, but they are expected to have a higher detection efficiency.

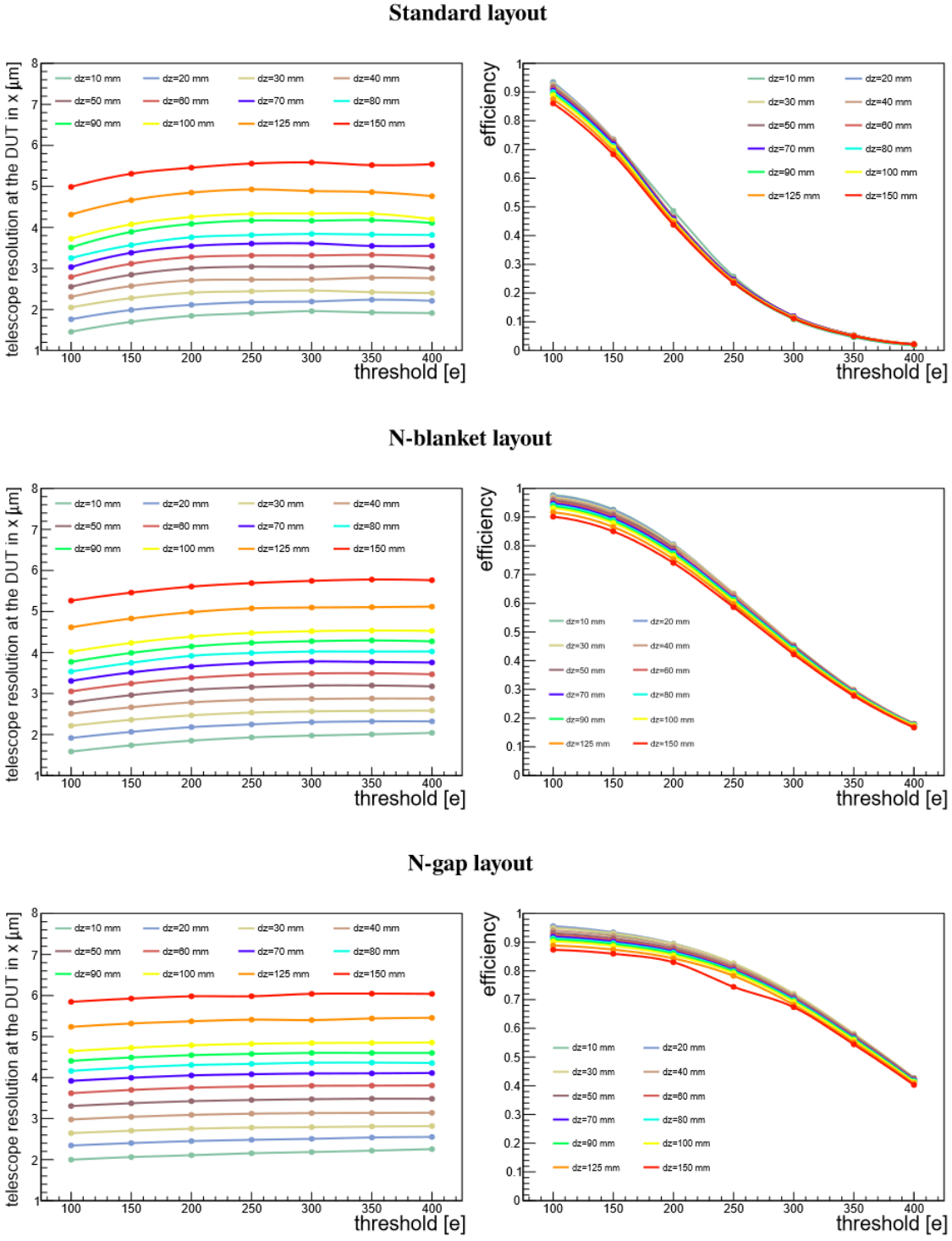

Figure 7.4: Telescope resolution at the DUT (left) and tracking efficiency (right) as a function of the detection threshold and distance between telescope planes, for the three different layouts (standard on the top, n-blanket in the middle and n-gap on the bottom).

The same effect can be observed in Figure 7.3(b), where three different detection thresholds are compared for the standard layout. By increasing the detection threshold, the cluster size is reduced, and the charge-weighted cluster reconstruction is applied to a small fraction of events. Therefore, at higher thresholds desired to reduce the noise, the telescope resolution deteriorates.

The combination of all these effects is shown in the first column of Figure 7.4. On the left side, the telescope resolution at the DUT position is shown as a function of the detection threshold and the distance between telescope planes for the three layouts. A smaller distance between telescope planes improves the tracking resolution for the detection thresholds. Furthermore, an increase in the detection threshold does not result in a large deterioration of the tracking resolution, as is the case of the intrinsic resolution of a sensor (see Figure 4.2).

7.3 Telescope efficiency

The tracking efficiency, defined as the fraction of events that are reconstructed (i.e. the reconstructed events divided by the total number of simulated events), is shown on the right side of Figure 7.4 for the three investigated layouts. It can be seen that the tracking efficiency at lower thresholds depends on the distance between telescope planes, being better for smaller distances, since scattering in air is reduced. At higher thresholds, all distances have similar efficiency, dominated by the low number of reconstructed events, resulting in low statistics and influencing the telescope resolution at the DUT position.

For a detection threshold of 200 electrons, the three different layouts are compared in Figure 7.5. The telescope resolution and tracking efficiency as a function of the distance between telescope planes are shown. As expected, the standard layout shows the best resolution. In comparison, the n-blanket and n-gap have slightly lower resolutions. However, this difference is smaller than in the sensors studies, meaning that placing sensor layers and performing tracking

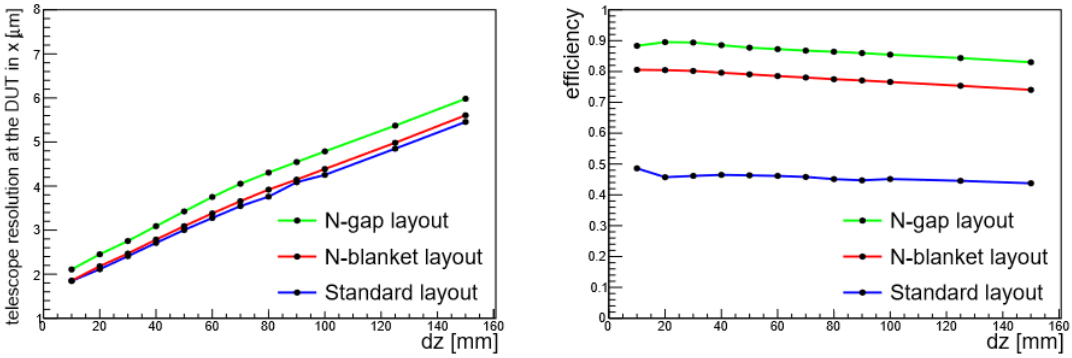

Figure 7.5: Telescope resolution at the DUT (left) and tracking efficiency (right) as a function of the distance between telescope planes for the three different layouts at a threshold of 200 electrons.

improves the spatial resolution (as expected from the basic function of a tracking detector, and in agreement with Figure 7.2(a)). The n-gap presents a superior tracking efficiency with respect to the other layouts. At this working detection threshold, the tracking efficiency is nearly constant for the different distances between telescope planes, while the spatial resolution deteriorates linearly with this distance.

7.4 Simulations with a larger pixel size

Up to now, all the simulations presented in this thesis have been performed with a pixel pitch of 20 µm. However, this pixel pitch might be too small to host the desired front-end in the Tangerine

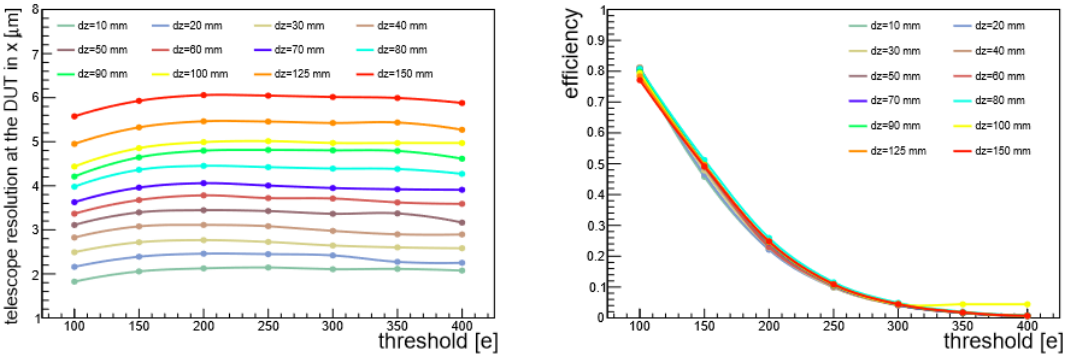

Figure 7.6: Telescope resolution at the DUT (left) and tracking efficiency (right) as a function of the detection threshold and distance between telescope planes, for the standard layout with a pixel pitch of 25 µm.

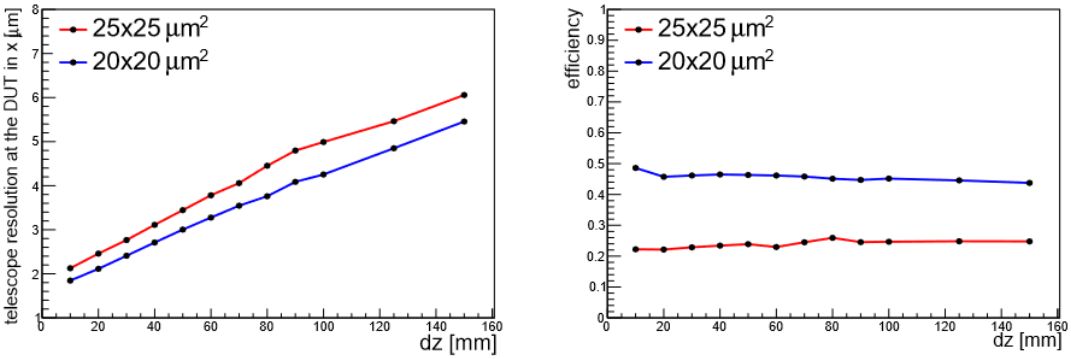

Figure 7.7: Telescope resolution at the DUT (left) and tracking efficiency (right) as a function of the distance between telescope planes for two different pixel pitches, 20 µm and 25 µm, at a threshold of 200 electrons. Simulations performed with the standard layout.

chips. Therefore, other pixel sizes are under investigation. In particular, in the work presented here, six parallel telescope planes consisting of pixellated sensors with a pitch of 25 µm with the standard layout are also simulated. For the other layouts, no fields for 25 µm pixel pitches were available yet. Figure 7.6 shows the comparison with respect to the 20 µm pitch for the standard layout with a detection threshold of 200 electrons. Larger pixel sizes deteriorate the resolution, and especially, the efficiency as shown in Figure 7.7. The loss in efficiency is expected to be smaller for the other layouts.

7.5 Full digitization stage

So far, only a simple digitization stage with a detection threshold has been applied. A more complete digitization stage can be simulated in the `DefaultDigitizer` module with Allpix^2. In particular, studies including the charge-to-digital converter in the simulations are presented in this section. The `DefaultDigitizer` module configuration used is given below, where `qdc_resolution` and `electronics_noise` are provided by the ASIC designers, and `qdc_slope` and `qdc_offset` are chosen as explained in Section 2.3.3.

```
[DefaultDigitizer]
electronics_noise = 35e
threshold = 100e
threshold_smearing = 0e
qdc_resolution = 6
qdc_slope = 20e
qdc_offset = -100
```

Figure 7.8(a) compares the biased residual widths for simple digitization (sd) in dashed lines where only the detection threshold is applied and more complete digitization (cd) in full lines with the charge-to-digital converter, for the standard layout with a pixel pitch of 20 µm. The intrinsic resolution of the sensor (in red) deteriorates by about 1.5 µm. As seen before, tracking recovers this degradation, and the difference between the simple and more complete digitization is reduced when tracking is involved (blue and green lines).

Moreover, the telescope resolution at the DUT position as a function of the distance between telescope planes is shown in Figure 7.8(b) for the two digitizations. For all distances, the difference between the resolution given by the simple and complete digitization is approximately 0.5 µm.

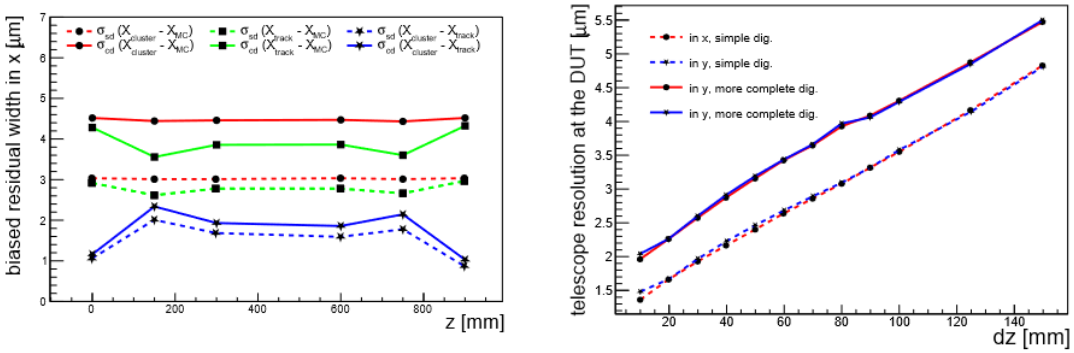

(a) (b)

Figure 7.8: (a) Biased residual widths between the cluster center and the Monte Carlo position, track intercept and Monte Carlo position, and cluster center and track intercept for each of the telescope planes for simple (sd, dashed lines) and more complete digitization (cd, full lines). (b) Telescope resolution at the DUT position for different distances between telescope planes for simple (sd, dashed lines) and more complete digitization (cd, full lines). Simulation performed with the standard layout with a detection threshold of 100 electrons and a pixel pitch of 20 µm.

7.6 Conclusion

Using the Allpix^2 and Corryvreckan frameworks for simulation and analysis, a full beam telescope has been simulated. The flexible simulations allowed for studies of the different design parameters and comparisons between the three sensor layouts under investigation.

As expected from sensor simulations, the simulated beam telescope based on the standard layout presented the best tracking performance. A telescope resolution in X at the DUT position below 3 µm is achieved at plane distances smaller than 50 mm, a hit detection threshold of 100 electrons and a pixel pitch of 20 µm.

Higher pixel pitches and detection thresholds are more realistic for the current prototype designs. However, the tracking resolution and efficiency have been observed to deteriorate by approximately 0.3 µm and a factor of two respectively for a pixel size of $25 \times 25\,\mu m^2$ for the standard layout compared to the $20 \times 20\,\mu m^2$.

The n-blanket and n-gap layouts have a higher efficiency than the standard layout. For the tracking definition given, an efficiency above 90 % for a detection threshold of 200 electrons is only maintained for the n-gap layout. The low tracking efficiency of the standard layout makes this layout not suitable in test beam facilities with a low rate.

Although the way in which the tracking efficiency is calculated allows for a good comparison between layouts, instead of using the total number of simulated events in the ratio, other

quantities could be more suitable. An alternative could be to perform a track reconstruction from the Monte Carlo positions and use this true number of reconstructed tracks instead of the total number of simulated events in the tracking efficiency definition. In this way, particles that are scattered and not crossing at least five telescope planes, or other discarded events due to cuts applied in the Corryvreckan reconstruction (see Section 3.7), will not affect the definition.

In general, the three sensor layouts investigated follow the same trend, meaning tracking resolution and efficiency deteriorate at higher thresholds and larger distances between beam telescope planes. The observed trends are consistent with measurements published for other beam telescopes. An example is the measurements of the EUDET-type beam telescopes based on MIMOSA26 sensors performed at DESY [27]. A direct comparison of the biased residual widths for all telescope planes presented in the publication and in this work can be done. A slightly better resolution is achieved with the sensors investigated in this thesis for all telescope planes.

Summary and Outlook

Summary

Within the Tangerine Project, many studies are ongoing to demonstrate the capabilities of the 65 nm CMOS imaging technology in high energy physics. All the simulations that are being carried out provide valuable insight into the sensors, broadening the knowledge of this novel technology and improving the design of new prototypes. Characterization of new prototypes and comparison with sensor simulations is one of the primary goals.

In this thesis, starting from three-dimensional TCAD simulations of the pixel cells, a full beam telescope based on a novel 65 nm CMOS imaging technology has been successfully simulated with Allpix^2. While TCAD provides very accurate insight of the sensor, its main limitation is the high computational cost (RAM and time). Thus, the high-statistic studies needed for sensor characterization are not practical using only TCAD. Allpix^2 exploits the doping profiles and electric fields simulated with TCAD and provides fast, precise, and high statistics Monte Carlo simulations of a full beam telescope setup. Moreover, the Corryvreckan framework allows for flexible and fast test beam data reconstruction. In summary, the combination of TCAD, Allpix^2, and Corryvreckan results in a very powerful, fast, and flexible tool for the simulation and analysis of beam telescopes.

Different sensor layouts and beam telescope geometries have been tested. In general, smaller distances between beam telescope planes, small pixel pitches, and low thresholds (maintaining a high signal-to-noise ratio) are preferred. Differences between them are compatible with the sensors simulations [21] and results from other simulation tools [40]. Furthermore, all the trends observed are consistent with measurements performed with beam telescopes [27].

Moreover, parameters included in the simulations with Allpix^2 have been tested and validated. The performance of the sensors investigated in high density scenarios has been studied as well, concluding that one-particle events can be distinguished from two-particle events with a misclassification rate of approximately 20 %. No significant difference was observed for the three examined layouts in this regard.

Outlook

Exploiting the flexibility of Allpix^2, scans over different parameters can be done, extending the results presented in this work. Tracking performance for different material budgets of the DUT,

variations of the distance from the DUT to the nearest telescope planes, and different beam energy scans are some of the possible studies. Different pixel sizes and geometries (for example, rectangular or hexagonal pixels) and different bias voltages at which the detectors can be operated can be investigated as well.

Furthermore, having observed that tracking mitigates the deterioration of resolution of the n-gap layout at higher thresholds and maintains its high efficiency, a dedicated analysis of this layout can be done to optimize its tracking performance. Such an examination can include scans for different p-well opening and n-gap sizes.

Finally, the studies for high density situations could be improved by involving a more complex multivariable analysis if more variables are available.

APPENDIX A

Corryvreckan detector configuration example

An example of a Corryvreckan configuration file obtained with Allpix^2 before alignment corrections:

```
[telescope0]
position = -1.18744mm, -59.1333um, 24.0704um
orientation_mode = "xyz"
orientation = -0.225416deg, 0.33004deg, 179.71deg
type = "20um_pitch"
pixel_pitch = 20um, 20um
number_of_pixels = 1024, 1024
role = reference
material_budget = 0.000533842

[telescope1]
position = 1.74409mm, 194.769um, 149.884mm
orientation_mode = "xyz"
orientation = 0.305186deg, -0.48759deg, -180deg
type = "20um_pitch"
pixel_pitch = 20um, 20um
number_of_pixels = 1024, 1024
material_budget = 0.000533842

[telescope2]
position = -1.26851mm, -1.11012mm, 299.896mm
orientation_mode = "xyz"
orientation = -0.281179deg, -0.194058deg, -179.984deg
type = "20um_pitch"
pixel_pitch = 20um, 20um
number_of_pixels = 1024, 1024
material_budget = 0.000533842
```

```
[telescope3]
position = -1.68633mm, 241.99um, 600.008mm
orientation_mode = "xyz"
orientation = 0.12525deg, 0.265906deg, -179.945deg
type = "20um_pitch"
pixel_pitch = 20um, 20um
number_of_pixels = 1024, 1024
material_budget = 0.000533842

[telescope4]
position = 788.447um, 880.876um, 749.971mm
orientation_mode = "xyz"
orientation = 0.148488deg, 0.165181deg, 179.98deg
type = "20um_pitch"
pixel_pitch = 20um, 20um
number_of_pixels = 1024, 1024
material_budget = 0.000533842

[telescope5]
position = -1.14033mm, -12.135um, 900.004mm
orientation_mode = "xyz"
orientation = 0.0691212deg, -0.0505393deg, -179.596deg
type = "20um_pitch"
pixel_pitch = 20um, 20um
number_of_pixels = 1024, 1024
material_budget = 0.000533842
```

Bibliography

[1] *Technology Computer Aided Design (TCAD) - Synopsys*, Accessed: 10-10-2022, URL: https://www.synopsys.com/silicon/tcad.html (cit. on p. 1).

[2] S. Spannagel et al., *Allpix^2: A modular simulation framework for silicon detectors*, Nuclear Instruments and Methods in Physics Research Section A: Accelerators, Spectrometers, Detectors and Associated Equipment **901** (2018) 164, URL: https://doi.org/10.1016%2Fj.nima.2018.06.020 (cit. on pp. 1, 11–13, 41).

[3] D. Dannheim et al., *Corryvreckan: a modular 4D track reconstruction and analysis software for test beam data*, Journal of Instrumentation **16** (2021) P03008, URL: https://doi.org/10.1088%2F1748-0221%2F16%2F03%2Fp03008 (cit. on pp. 1, 11, 23, 30).

[4] H. Kolanoski and N. Wermes, *Particle Detectors*, Oxford University Press, 2020, ISBN: 978-0-19-885836-2 (cit. on pp. 3, 5, 8, 9).

[5] R. L. Workman et al., *Review of Particle Physics*, PTEP **2022** (2022) 083C01 (cit. on pp. 3, 4, 7, 21).

[6] L. D. Landau, *On the energy loss of fast particles by ionization*, Journal of Physics **8** (1944) 201, URL: https://cds.cern.ch/record/216256 (cit. on p. 4).

[7] P. Hofmann, *Solid State Physics: An Introduction*, Wiley, 2015, ISBN: 9783527682034, URL: https://books.google.de/books?id=z6ycCQAAQBAJ (cit. on p. 5).

[8] C. Jacoboni, C. Canali, G. Ottaviani and A. Alberigi Quaranta, *A review of some charge transport properties of silicon*, Solid-State Electronics **20** (1977) 77, ISSN: 0038-1101, URL: https://www.sciencedirect.com/science/article/pii/0038110177900545 (cit. on p. 7).

[9] C. Scharf and R. Klanner, *Measurement of the drift velocities of electrons and holes in high-ohmic 100 silicon*, Nuclear Instruments and Methods in Physics Research Section A: Accelerators, Spectrometers, Detectors and Associated Equipment **799** (2015) 81, ISSN: 0168-9002, URL: https://www.sciencedirect.com/science/article/pii/S0168900215008955 (cit. on p. 7).

[10] G. Masetti, M. Severi and S. Solmi, *Modeling of carrier mobility against carrier concentration in arsenic-, phosphorus-, and boron-doped silicon*, IEEE Transactions on Electron Devices **30** (1983) 764 (cit. on p. 7).

[11] N. Arora, J. Hauser and D. Roulston, *Electron and hole mobilities in silicon as a function of concentration and temperature*, IEEE Transactions on Electron Devices **29** (1982) 292 (cit. on p. 7).

[12] K. Wolters, S. Spannagel and D. Hynds, *User Manual for the Allpix^2 Simulation Framework*, Accessed: 15-10-2022, URL: https://cern.ch/allpix-squared/usermanual/allpix-manual.pdf (cit. on pp. 7, 8, 13).

[13] W. Shockley and W. T. Read, *Statistics of the Recombinations of Holes and Electrons*, Physical Review **87** (1952) 835 (cit. on p. 8).

[14] J. Fossum and D. Lee, *A physical model for the dependence of carrier lifetime on doping density in nondegenerate silicon*, Solid-State Electronics **25** (1982) 741, ISSN: 0038-1101, URL: https://www.sciencedirect.com/science/article/pii/0038110182902039 (cit. on p. 8).

[15] L. Rossi, P. Fischer, T. Rohe and N. Wermes, *Pixel Detectors: From Fundamentals to Applications*, Particle Acceleration and Detection, Berlin: Springer-Verlag, 2006, ISBN: 978-3-540-28332-4, 978-3-540-28333-1 (cit. on p. 8).

[16] W. Snoeys et al., *A process modification for CMOS monolithic active pixel sensors for enhanced depletion, timing performance and radiation tolerance*, Nuclear Instruments and Methods in Physics Research Section A: Accelerators, Spectrometers, Detectors and Associated Equipment **871** (2017) 90, ISSN: 0168-9002, URL: https://www.sciencedirect.com/science/article/pii/S016890021730791X (cit. on pp. 9, 35, 38).

[17] M. Munker et al., *Simulations of CMOS pixel sensors with a small collection electrode, improved for a faster charge collection and increased radiation tolerance*, Journal of Instrumentation **14** (2019) C05013, URL: https://doi.org/10.1088/1748-0221/14/05/c05013 (cit. on pp. 9, 35, 36, 38).

[18] M. Mager, *ALPIDE, the Monolithic Active Pixel Sensor for the ALICE ITS upgrade*, Nuclear Instruments and Methods in Physics Research Section A: Accelerators, Spectrometers, Detectors and Associated Equipment **824** (2016) 434, Frontier Detectors for Frontier Physics: Proceedings of the 13th Pisa Meeting on Advanced Detectors, ISSN: 0168-9002, URL: https://www.sciencedirect.com/science/article/pii/S0168900215011122 (cit. on pp. 9, 35).

[19] M. Buckland,
Development of the ITS3: A bent-silicon vertex detector for ALICE in the LHC Run 4,
Nuclear Instruments and Methods in Physics Research Section A: Accelerators, Spectrometers, Detectors and Associated Equipment **1039** (2022) 166875,
ISSN: 0168-9002, URL:
https://www.sciencedirect.com/science/article/pii/S0168900222003436
(cit. on p. 10).

[20] A. Simancas, *Device simulations of a MAPS in 65 nm CMOS Imaging Technology dedicated for test beam measurements*,
(20-24/6/2022), 10th Beam Telescopes and Test Beams Workshop,
URL: https://indico.cern.ch/event/1058977/contributions/4636892
(cit. on pp. 11, 42).

[21] H. Wennlöf et al.,
The Tangerine project: Development of high-resolution 65 nm silicon MAPS,
Nuclear Instruments and Methods in Physics Research Section A: Accelerators, Spectrometers, Detectors and Associated Equipment **1039** (2022) 167025,
ISSN: 0168-9002, URL:
https://www.sciencedirect.com/science/article/pii/S0168900222004508
(cit. on pp. 12, 35, 69).

[22] S. Agostinelli et al., *Geant4—a simulation toolkit*,
Nuclear Instruments and Methods in Physics Research Section A: Accelerators, Spectrometers, Detectors and Associated Equipment **506** (2003) 250, ISSN: 0168-9002,
URL:
https://www.sciencedirect.com/science/article/pii/S0168900203013688
(cit. on p. 12).

[23] J. Apostolakis et al., *An implementation of ionisation energy loss in very thin absorbers for the GEANT4 simulation package*,
Nuclear Instruments and Methods in Physics Research Section A: Accelerators, Spectrometers, Detectors and Associated Equipment **453** (2000) 597, ISSN: 0168-9002,
URL:
https://www.sciencedirect.com/science/article/pii/S0168900200004575
(cit. on p. 17).

[24] E. Fehlberg, *Low-order classical Runge-Kutta formulas with stepsize control and their application to some heat transfer problems*, (1969),
URL: http://hdl.handle.net/2060/19690021375 (cit. on p. 19).

[25] R. Diener et al., *The DESY II test beam facility*,
Nuclear Instruments and Methods in Physics Research Section A: Accelerators, Spectrometers, Detectors and Associated Equipment **922** (2019) 265, ISSN: 0168-9002,
URL:
https://www.sciencedirect.com/science/article/pii/S0168900218317868
(cit. on p. 23).

[26] R. Turchetta, *Spatial resolution of silicon microstrip detectors*, Nuclear Instruments and Methods in Physics Research Section A: Accelerators, Spectrometers, Detectors and Associated Equipment **335** (1993) 44, ISSN: 0168-9002, URL: https://www.sciencedirect.com/science/article/pii/016890029390255G (cit. on p. 25).

[27] H. Jansen et al., *Performance of the EUDET-type beam telescopes*, EPJ Techniques and Instrumentation **3** (2016), URL: https://doi.org/10.1140%2Fepjti%2Fs40485-016-0033-2 (cit. on pp. 27, 67, 69).

[28] R. E. Kalman, *A New Approach to Linear Filtering and Prediction Problems*, Journal of Basic Engineering **82** (1960) 35, ISSN: 0021-9223, eprint: https://asmedigitalcollection.asme.org/fluidsengineering/article-pdf/82/1/35/5518977/35_1.pdf, URL: https://doi.org/10.1115/1.3662552 (cit. on p. 29).

[29] C. Kleinwort, *General broken lines as advanced track fitting method*, Nuclear Instruments and Methods in Physics Research Section A: Accelerators, Spectrometers, Detectors and Associated Equipment **673** (2012) 107, URL: https://doi.org/10.1016%2Fj.nima.2012.01.024 (cit. on p. 29).

[30] F. James and M. Roos, *Minuit - a system for function minimization and analysis of the parameter errors and correlations*, Computer Physics Communications **10** (1975) 343, ISSN: 0010-4655, URL: https://www.sciencedirect.com/science/article/pii/0010465575900399 (cit. on p. 30).

[31] J. Kröger, S. Spannagel and M. Williams, *Corryvreckan User Manual*, Accessed: 20-10-2022, URL: http://cern.ch/go/db9Z. (cit. on p. 30).

[32] A. Chauhan et al., *Towards a New Generation of Monolithic Active Pixel Sensors*, 2022, URL: https://arxiv.org/abs/2210.09810 (cit. on p. 35).

[33] S. Senyukov et al., *Charged particle detection performances of CMOS pixel sensors produced in a* 0.18 µm *process with a high resistivity epitaxial layer*, Nuclear Instruments and Methods in Physics Research Section A: Accelerators, Spectrometers, Detectors and Associated Equipment **730** (2013) 115, URL: https://doi.org/10.1016%2Fj.nima.2013.03.017 (cit. on pp. 35, 38).

[34] *Geant4 Collaboration*, Accessed: 10-10-2022, URL: https://geant4.web.cern.ch/node/302 (cit. on p. 43).

[35] M. A. del Rio Viera, *Tangerine: Monte Carlo simulations of MAPS in a 65 nm imaging process*, (20-24/6/2022), 10th Beam Telescopes and Test Beams Workshop, URL: https://indico.cern.ch/event/1058977/contributions/4631484 (cit. on p. 46).

[36] R. Jacobs, *LUXE: A new experiment to study non-perturbative QED in electron-LASER and photon-LASER collisions*, 2022, URL: https://arxiv.org/abs/2205.06096 (cit. on p. 51).

[37] H. Abramowicz et al., *Conceptual design report for the LUXE experiment*, The European Physical Journal Special Topics **230** (2021) 2445, URL: https://doi.org/10.1140%2Fepjs%2Fs11734-021-00249-z (cit. on p. 51).

[38] Y. Coadou, *Boosted Decision Trees and Applications*, EPJ Web Conf. **55** (2013) 02004, ed. by T. Delemontex and A. Lucotte (cit. on p. 57).

[39] *TMVA - Machine learning with ROOT*, Accessed: 10-10-2022, URL: https://root.cern/manual/tmva/ (cit. on p. 57).

[40] S. Kulis. and D. Dannheim, *Telescope resolution calculator*, Accessed: 10-10-2022, 2014, URL: http://skulis.web.cern.ch/skulis/telescope/ (cit. on p. 69).

List of Figures

List of Tables

Acknowledgements

I am extremely grateful to Simon Spannagel for giving me the opportunity to work under his supervision on this interesting topic. Thank you very much Simon for all your teaching, patience when my brain is 100 times slower than yours, opportunities, and trust that you have always placed in me.

I would like to extend my deepest gratitude to Håkan Wennlöf for his brilliant supervision of this project, encouragement, and invaluable teaching at all the stages. Thank you very much Håkan, and I am sorry for the many times I went to your office with simulation problems, stupid mistakes, and millions of questions.

Thank you to Adriana, Daniil, Finn, Gianpiero, Håkan, Larissa, Lennart, Manuel, Naomi, Nastya, Paul, Simon, Stephan, and Tangy, for all the interesting discussions and contributions to this thesis. I am extremely grateful to be part of this great team.

I am also grateful to the entire ATLAS-DESY group for all the social activities, lunches, and cakes. I can not mention all of you by name but be assured you are equally and deeply acknowledged.

I would like to express my gratitude to Prof. Ingrid Gregor and Prof. Jochen Dingfelder for immediately agreeing to be the examiners of this work, teaching, and warm welcomes in their amazing groups.

Finally, I can not thank my family and friends enough for their unconditional support.